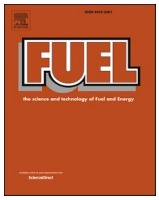
Fuel 407 (2026) 137354



Contents lists available at ScienceDirect

Fuel

journal homepage: www.elsevier.com/locate/fuel



Full Length Article



Steam reforming of levulinic acid as a model compound of bio-oil from the hydrothermal liquefaction of biomass

Sergi López, Francesc Xavier Lara, Francesc Medina, Magdalena Constantí, Daniel Montané *

Universitat Rovira i Virgili. Departament d'Enginyeria Química. Av. dels Països Catalans, 26. 43007 Tarragona, Spain

ARTICLE INFO

Keywords:
Levulinic acid
Hydrogen
Steam reforming
Layered double hydroxides
Hydrothermal liquefaction
·Carbon deposition

ABSTRACT

Hydrothermal liquefaction (HTL) of wet and lignocellulosic biomass yields bio-oil and an aqueous phase rich in furans, aldehydes, ketones, organic acids, and phenolics. Bio-oil can be used as a drop-in fuel after hydrotreatment to enhance its energy density and compatibility with conventional fuels. Steam reforming (SR) of the aqueous phase has been proposed to source hydrogen for hydrotreating the bio-oil. Despite levulinic acid (LA) being a main cellulose-derived product in the aqueous phase of HTL, information on its steam reforming is limited. In this work, we studied the SR of LA on Ni/Mg-Al catalysts obtained from hydrotalcite-like precursors, both unpromoted and promoted with Zr and Ce. The catalysts were synthesized by coprecipitation and calcination at 450, 600 and 750 °C, and activated by reduction at 600 °C. Activity was tested for 16 h at 500 and 600 °C at steam-to-carbon molar ratios (S/C) of 2.4, 5.4 and 8.4. Filamentous and multilayered carbon structures were observed in the unpromoted catalysts, especially at the lower temperature and S/C ratios. Promotion with Zr decreased coking resistance and increased the formation of carbon filaments. Addition of CeO_2 reduced the extent of coking, but still multilayered carbon deposits and whiskers were formed. A Ce-promoted catalyst maintained constant activity for 100 h at 600 °C, S/C of 8.4, and $WHSV_{LA}$ of 6.47 h^{-1}, achieving complete LA conversion, a fractional yield of hydrogen of 0.91, and selectivity to carbon dioxide, carbon monoxide and methane of 0.83, 0.11 and 0.01, with a carbon balance closure above 96 %.

1. Introduction

The environmental impact of fossil fuels and the growing energy demand have driven the search for alternative fuels for transportation and industry. Biomass, as a unique source of biogenic carbon, can contribute to the substitution of fossil resources. Among several routes, fast pyrolysis (FP) and hydrothermal liquefaction (HTL) can convert biomass into liquid fuel precursors [1,2]. FP at near atmospheric pressure and 450 – 550 °C is suitable for dry lignocellulosic biomass like wood, straws, and agriculture by-products [3,4]. HTL proceeds in aqueous environment at 5 – 20 MPa and 250 – 350 °C, and it is better suited for wet biomass such as algae, food-processing waste, animal manure and sewage sludge, but it can process lignocellulosic feedstocks as well [4,5]. Both processes give variable yields of gas, char, and liquid products depending on the type of biomass, temperature, the use of catalysts, and in HTL the use of solvents different from water [2]. The liquid fraction, commonly referred to as biocrude or bio-oil, is the desired product in both processes. Bio-oil is a complex mixture formed by the thermochemical depolymerization of the biomass constituents. It includes aromatics from lignin, anhydro sugars, furans, aldehydes, ketones and organic acids from cellulose and hemicellulose, and in microalgae and other wet biomasses, fatty acids and long chain hydrocarbons evolving from oils and fats [4,6]. Comparative studies have shown that FP and HTL bio-oils differ in composition and properties. HTL bio-oils have better quality and stability [1,7,8] since they are less oxygenated and have a higher energy density [9]. FP oil is unstable upon storage because ketones and phenolic monomers repolymerize with pyrolytic lignin rising the viscosity [10–12]. Aged bio-oil splits into a viscous tarry phase consisting of phenolics and lignin aromatics, and an aqueous phase (APh) that concentrates organic acids, anhydro sugars, and low molar mass polar compounds [10,12]. Since HTL is conducted in aqueous media, it directly splits into aqueous and organic phases [4]. The latter constitutes the bio-oil, but the aqueous phase is rich in polar compounds derived from carbohydrates. In addition, the HTL of

* Corresponding author.
E-mail address: daniel.montane@urv.cat (D. Montané).

https://doi.org/10.1016/j.fuel.2025.137354
Received 24 July 2025; Received in revised form 17 October 2025; Accepted 26 October 2025
Available online 30 October 2025
0016-2361/© 2025 The Author(s). Published by Elsevier Ltd. This is an open access article under the CC BY-NC-ND license (http://creativecommons.org/licenses/by-nc-nd/4.0/).

biomasses containing lipids produce bio-oils rich in fatty acids and long-chain hydrocarbons. Bio-oils from HTL are generally unstable, although their aging characteristics strongly depend on the biomass [13]. Even if many of the compounds present in FP and HTL bio-oils are valuable platform chemicals, their recovery is not economical given the low concentrations at which they are present. Consequently, the envisaged use of bio-oil is as drop-in fuel. FP and HTL bio-oils are unsuitable as fuels due to their immiscibility with conventional liquid fuels, inferior physicochemical properties, and lower energy density compared to conventional fuels [2]. Hydrotreating and hydrocracking are effective techniques to upgrade bio-oil. Hydrotreating increases the energy density and reduces the oxygen content, and it lowers the organically bound nitrogen in oils produced from high protein biomasses. Hydrotreating of the bio-oil obtained by HTL of lipid-rich biomass holds promise to produce biofuels within the kerosene range [14]. Hydrocracking reduces viscosity by breaking down the larger fragments of pyrolytic lignin into smaller molecules [2,9,15]. The hydrogen needed for both processes can be obtained by steam reforming (SR) either a fraction of the bio-oil, or the aqueous phase decanted from the bio-oil [2,9,16,17]. The latter is interesting as it valorizes the aqueous phase and does not consume additional feedstocks to rise hydrogen [18].

Steam reforming of fast pyrolysis bio-oil and its aqueous phase has proven challenging due to rapid catalyst deactivation, and many studies have focused on model compounds to investigate the underlying phenomena. Catalysts based on nickel are the most common, but other metals active for the steam reforming of hydrocarbons such as Co and Rh have been studied as well. Those metals have been also tested as nickel promoters in bimetallic catalysts. Common support materials include alumina, lanthanum oxide, cerium oxide, magnesium oxide and zinc oxide, and mixed oxides obtained by impregnation with support modifiers or synthesized by coprecipitation techniques. The main difficulty in SR of whole bio-oil or bio-oil APh is carbon deposition. This is a complex phenomenon that must be controlled to prevent a rapid deactivation of the catalyst. The underlying mechanisms of carbon deposition during bio-oil and APh steam reforming are equivalent to those of methane and higher hydrocarbons. The extent of catalyst coking depends on the nature of the organic feedstock, the characteristics of the catalytic surface, the availability of water (S/C ratio), and temperature. The combination of those factors determines not only the rate of carbon accumulation but the morphology and the structure of the deposited carbon as well. Highly oxygenated and reactive compounds such as anhydro sugars form amorphous pyrolytic carbon by thermal cracking in the gas phase at high temperature that results in the blockage of the catalyst bed even if the catalyst surface is clean of carbon deposits, while at lower temperature they polymerize encapsulating the catalyst with amorphous carbon [19,20]. Furans and aromatics polymerize on the catalyst surface and form encapsulating carbon that passivates the catalyst [21–23]. Aliphatic compounds such acetic acid tend to form aromatic carbon filaments and graphitic whiskers [19,24–28]. Those do not cause rapid deactivation, but the whiskers growing inside the porous structure of the catalyst exert compressive forces that finally disintegrate the particles and cause an increase of pressure drop in the reactor. The type of carbon, and not the sheer quantity, is therefore the key factor concerning deactivation during SR of FP bio-oil. The availability of water adsorbed on the surface of the catalyst plays a crucial role in favoring the production of hydrogen gas over carbon monoxide or methane and facilitates the gasification of carbon precursors. The steam-to-carbon ratio (S/C) determines the partial pressure of water in the gas, but the water affinity of the surface is equally important. Modifiers and promoters that increase the availability of oxygen vacancies in the catalyst surface like CeO_2, La_2O_3, ZnO, MgO or SiO_2 increase steam adsorption and favor the gasification of the deposited coke [28–39]. The basicity and acidity of the support phase play a significant role in catalyst coking. Surfaces with strong acidic and basic centers promote dehydration, ketonization, and condensation reactions of the adsorbed oxygenated organics, which results on the formation of encapsulating carbon [31,35,40–42], but the presence of weak basic sites is beneficial to improve the gasification of the deposited carbon [43]. Regarding the active phase, Ni tends to produce carbon filaments and whiskers, while Co and especially Rh tend to form encapsulating deposits [25,34,44]. The formation of carbon whiskers can be reduced in nickel catalysts using modifiers and promoters that favor the dispersion of the metal and the formation of small metal particles upon reduction. Temperature is the most influential parameter in SR, but it must be adjusted to balance the processes influencing catalyst activity and its deactivation rate. In general, temperature reduces coking and increases the yield of hydrogen by promoting the rate of gasification of the deposited carbon [20,21,45], but the effect of temperature on coking depends on the active metal [25]. Temperature makes the carbon deposits more polyaromatic and olefinic and less aliphatic and oxygenated [23]. However, excessive temperatures may produce amorphous pyrolytic carbon by thermal cracking of the feedstock [25]. Sintering is also a concern in SR catalysts, particularly due to the high temperatures typically needed for reforming and the presence of superheated steam. However, sintering may not be readily observable in practice because coke deposition deactivates the catalyst well before sintering becomes evident. To reduce sintering, operation temperatures significantly above the Tammann temperature of the active phase should be avoided [46]. Sintering has been repeatedly reported in Ni-based catalysts for bio-oil SR above 600 °C [36,37,44,47,48]. Susceptibility to sintering can be reduced with modifiers that increase the interaction with the support [28,33,47,48] or by using metal promoters that form metal alloys with Ni [37,49], which may also improve the dispersion of the metal [38]. Rh based catalysts can withstand operation temperatures as high as 800 °C with minimum sintering [25].

In contrast to the abundant literature on the steam reforming of FP bio-oil, the production of hydrogen by steam reforming of HTL bio-oil and its aqueous fraction has been less studied. Park et al. [50] investigated the SR of desalted bio-oil from the HTL of *Saccharina japonica* on a 17 % $Ni/SrTiO_3$ catalyst. At 800 °C and S/C 15.8 the catalyst achieved stable operation for 20 h and it produced a higher yield of hydrogen and accumulated less carbon than a Ni/Al_2O_3 catalyst with the same nickel content. This was attributed to a larger amount of reactive lattice oxygen that favored the conversion of carbon monoxide to carbon dioxide and hydrogen. In another study from the same group, desalted bio-oil from the HTL of *Saccharina japonica* was steam reformed using several $Ni_xCu_{(1-x)}Mg_{1.5}Al_{1.0}$ hydrotalcite-derived catalysts [49]. A catalyst containing a 1:1 Ni:Cu atomic ratio maximized hydrogen production with a H_2/CO ratio of 28 in the reformate gas at 750 °C and a S/C of 10, and it was stable for 5 h TOS without substantial coke deposition. Those results demonstrate the feasibility of reforming the aqueous phase of HTL bio-oil to produce hydrogen, but they are limited to bio-oil from a single source of aquatic biomass. SR of HTL bio-oils produced from other wet biomasses and lignocellulosic wastes may pose additional challenges compared to FP bio-oil due to differences in composition caused by the dissimilar reaction environments. The presence of an aqueous phase at high pressure during HTL modifies the reaction pathways involved in the conversion of cellulose and hemicellulose with respect to those of FP [4]. In a comparative study using beech wood between FP in a cyclone reactor and HTL in a conventional autoclave, Doassans-Carrère et al. [8] observed several compositional differences in the bio-oil and the aqueous fraction. Notably, the main products from cellulose were levoglucosan in FP and levulinic acid (LA) in HTL. Moreover, the latter was absent in the aqueous phase of FP, while levoglucosan was not amongst the products of HTL. Lu et al. [51] reported the formation of LA as the main carboxylic acid in the HTL of residues from the bioethanol fermentation of reed and corn stover, along with acetic and propionic acids. Lee and coworkers reported the formation of LA during the HTL of coconut shells [52] and empty fruit bunches [53] using $CuCl_2$ as catalyst. In the HTL of several lipid-rich algae and microalgae LA was also one of the main products in the aqueous phase [6,18].

There is little information in the literature about the steam reforming

of levulinic acid. To the best of our knowledge, only two recent studies by the same group have been published. Li et al. [54] achieved almost complete conversion of LA to gases and a hydrogen yield of 92.8 % at 800 °C and a S/C ratio of 24 during 40 h with a catalysts containing 15 wt% of Ni supported on a $NiAl_2O_4$ spinel. The high yield of hydrogen can be explained by the large S/C ratio that was used, which displaced the water gas shift and methanation reactions towards the formation of hydrogen. Even at this high S/C ratio, carbon deposition was observed on the catalyst by SEM imaging and XRD after 40 h of operation, but the amount and type of carbon deposited on the catalyst were not reported. In a subsequent paper by the same group, Su et al. [55] addressed the steam reforming of mixtures of levulinic acid with formic acid and furfural using the same catalyst and studied the influence of trace amounts of sulfuric acid on its deactivation. Addition of Cu or Co to produce Ni-M/$NiAl_2O_4$ bimetallic catalysts improved their resistance to the presence of the sulfuric acid, and a stable reforming activity was achieved at 800 °C and a S/C of 12. Given the limited data available on the steam reforming of levulinic acid and the high temperatures and S/C ratios required on the published works, in this paper we have investigated a Ni/Mg-Al layered double hydroxide precursor, both unpromoted and promoted with Zr and Ce, to obtain a catalyst that was active and stable at milder reforming conditions. Addition of Mg as support modifier to the Ni/Al system was considered since it enhances the basicity of the support and improves water adsorption and OH mobility, thus reducing coking during the steam reforming of acetic acid [25,30,35] and FP bio-oil [22,32,36]. Promotion with ZrO_2 changes the acidic/basic characteristics of the support and enhances the adsorption of steam and carbon oxides [33], while its high oxygen vacancies and redox capability favor the oxidation of carbon deposits [41]. Ce is an effective promoter in Ni/Al catalysts during the SR of oxygenated molecules. It enhances the dispersion of the active Ni phase upon reduction while cerium oxides provide oxygen mobility that contributes to water adsorption and facilitate the oxidation of dehydrogenated carbon species deposited on the surface [30,32,34,36,39]. We have studied the influence of the temperature of calcination of the LDH precursors and the addition of Zr and Ce as promoters on the structure and activity of the Ni/Mg-Al catalyst. The activity has been assessed in SR experiments at atmospheric pressure using S/C molar ratios from 2.4 to 8.4 and temperatures of 500 and 600 °C. The study has also focused on the characteristics of the carbon deposited on the catalysts. Finally, an extended test of 100 h has been conducted to demonstrate the stability of the Ce-promoted catalyst at 600 °C at a S/C ratio of 8.4.

2. Materials and methods

2.1. Synthesis of the catalysts

The catalysts were obtained by calcination and reduction of double layered hydroxides (LDH) precursors prepared by coprecipitation at controlled pH. The precursors had atomic ratios of Ni:Mg:Al of 2:1:1. To synthesize the LDH, 100 mL of a solution containing 1 mol·L^{-1} of Ni $(NO_3)_2$·6 H_2O (98 % purity, Thermo Scientific), 0.5 mol·L^{-1} of Mg $(NO_3)_2$·6 H_2O (extra pure, Thermo Scientific and 0.5 mol·L^{-1} of Al $(NO_3)_3$·9 H_2O (98 % purity, Fisher Scientific) were added dropwise to a 100 mL 0.30 mol·L^{-1} Na_2CO_3 (99.5 % purity, Fisher Scientific) solution under constant stirring. The pH of the mixture was controlled to 10 ± 0.5 by the addition of a 2 mol·L^{-1} in NaOH (98 % purity, PANREAC) solution. The resulting suspension was aged at 60 °C for 18 h. The solid product was separated by vacuum filtration, it was washed thoroughly several times with deionized water until the washings had a pH of 7, and it was dried at 100 °C for 12 h. The resulting LDH was then ground into a powder before undergoing calcination at 450, 600 or 750 °C for 5 h in static air. The calcined materials were labeled *HTn*, where *n* represented the calcination temperature in degrees Celsius (for instance, HT450). The catalysts containing zirconia were synthesized following the same procedure but adding 0.03 mol·L^{-1} of $ZrO(NO_3)_2$··H_2O (technical grade, Sigma Aldrich) to the solution of nickel, magnesium and aluminum nitrates to produce a LDH precursor with a nominal atomic ratio of Ni:Mg:Al:Zr of 2:1:0.95:0.05. The precursor was calcined at 450, 600 or 750 °C for 5 h in static air, and the calcined materials were labelled *HTn/Zr* (for example, HT450/Zr). The ceria-promoted catalysts were prepared by incipient wetness impregnation of the calcined HT450. Two catalysts containing 0.12 and 0.40 atom % of Ce were synthesized, which correspond to 0.33 and 1.32 metal mass %. Those values were selected based on the work of Bimbela et al. [32], who established that a 0.5 mass % of Ce gave the best result for the steam reforming of the aqueous phase of FP oil on Ni-Ce/MgAl catalysts. The materials were prepared by adding a solution of $(NH_4)_2[Ce(NO_3)_6]$ (98.5 % purity, Sigma-Aldrich) dropwise to a sample of calcined HT450. The concentration of nitrate and the volume of solution added were based on the total pore volume of the calcined material. After impregnation, the solid was dried at 100 °C for 12 h and it was calcined at 450 °C for 5 h in static air. The calcined materials were labelled HT450/Ce1 (0.1 atom % of Ce) and HT450/Ce4 (0.4 atom % of Ce). The active forms of the catalysts were obtained by reducing the calcined materials in a tubular reactor. The samples were heated at 10 °C·min^{-1} from room temperature to 600 °C and kept for 18 h under a constant flowrate of 10 mL_n·min^{-1} of hydrogen. If the catalyst sample was intended for characterization, the reduced catalyst was then cooled down to room temperature under 20 mL_n·min^{-1} of nitrogen. Once cold, the reactor was flooded with ethanol and disassembled, and the catalyst suspension was transferred to a vial that was sealed to prevent the reoxidation of nickel by contact with air. If the catalyst sample was intended for activity testing, it was first mixed with silica particles as described in section 2.3 and reduced following the same protocol. The reduced catalysts were labelled adding −*R* to their tag (for instance, HT450/Ce4-R).

2.2. Characterization of the catalysts

The textural properties of the catalysts were determined from the nitrogen adsorption–desorption isotherms at 77 K on a QuadraSorb SI Model 4.0 instrument with the QuadraWin Software (Quantachrome Instruments, v5.0). The samples were degassed under vacuum (6 mTorr) at 120 °C for 18 h before analysis in the instrument pre-chamber (FloVac Degasser, Quantachrome Instruments) to remove the adsorbed species. The surface area was calculated with the BET model, while the BJH model was applied to the desorption branch of the isotherm to calculate the pore volume and the pore size distribution. Temperature-Programmed Reduction (TPR) was conducted on an Autochem 2920 chemisorption analyzer (Micromeritics) equipped with a cold trap containing isopropanol at − 90 °C and a TCD detector. Samples of ca. 100 mg of calcined materials were placed in a U-quartz microreactor and treated at 300 °C for 30 min under a constant flow of 30 mL·min^{-1} of He to remove adsorbed species, and subsequently cooled to 40 °C. Temperature was then rampled up to 800°C at 10°C·min^{-1} under a flow of 30 mL·min^{-1} of a 10 % H_2/Ar mixture. The hydrogen consumption was calculated from the TCD detector signal. The crystalline structure of the materials was analyzed by X-Ray Diffraction (XRD) using a Siemens D5000 diffractometer (Bragg-Brentano parafocusing geometry and vertical θ −θ goniometer) fitted with a curved graphite diffracted-beam monochromator, incident and diffracted-beam Soller slits, a 0.06° receiving slit and scintillation counter as a detector. The angular 2 θ diffraction range was between 5 and 80°. The data were collected with an angular step of 0.05° at 3 s per step and sample rotation. Cuk α radiation was obtained from a copper X-ray tube operated at 40 kV and 30 mA. Environmental scanning electron microscopy (ESEM) was conducted with a Quanta 600 instrument (FEI Company). Field emission scanning electron microscopy (FESEM) was performed on a Scios-2 instrument (ThermoFisher) under high vacuum. Transmission electron microscopy (TEM) images were acquired using a JEOL 1011 TEM operated at 100 kV. High-resolution transmission electron microscopy (HR-TEM) images were acquired using a JEOL J200 operated at 200 kV,

elemental analysis was performed with an EDS Centurio Detector. Raman spectra were recorded at ambient temperature using a Raman Renishaw InVia Spectrometer equipped with a confocal DM 2500 Leical optical microscope, a CCD detector, and a diode laser operating at 785 nm. The applied power of the laser beam focusing on the sample was 3 mW. The spectra were mesured in the 900–1900 cm^{-1} range in single scan with 30 s of exposure time. The basicity of the catalysts was investigated by temperature-programmed desorption of CO_2 (CO_2-TPD) on a Micromeritics AutoChem II 2920 chemisorption analyzer. Initially, the catalyst samples (200 mg) were loaded in the U-quartz microreactor and reduced at 600 °C for 120 min while flowing 30 mL·min^{-1} of a 10 % H_2/Ar mixture. Subsequently, the samples were cooled down to 70 °C and exposed to a flow of 30 mL·min^{-1} of 2.5 % CO_2/He for 45 min. After that, the samples were cooled down to 40 °C with He and until the detector signal was stable. The temperature was then ramped up to 600 °C at a rate of 10 °C·min^{-1} under a helium flow of 30 mL·min^{-1}. The desorbed CO_2 was measured using a thermal conductivity detector (TCD). The thermal decomposition characteristics of the carbon deposited on the spent catalysts was investigated by thermogravimetry analysis (TGA) in a Sensys Evo TG-DSC thermobalance (SETARAM) equipped with an online mass spectrometer detector (QMG-220, Pfeiffer Vacuum). Samples of ca. 10 mg of spent catalyst were heated at 10 °C·min^{-1} to 100 °C, held for 15 min to fully dry the sample, and then heated to 800 °C at 10 °C·min^{-1} under a total flowrate of air of 30 mL_n·min^{-1}. The combustion of the carbon deposits was monitored by the change in mass of the sample and the respons of carbon dioxide in the MS detector.

X-ray photoelectron spectroscopy (XPS) analysis was performed using an ProvenX-NAP (Specs Surface Nano Analysis GmbH, Berlin, Germany) spectrometer with a dual (AlKα = 1487 eV / AgLα = 2984 eV) monochromatic X-ray source (μFocus450). The measurements were collected under these conditions: power of X-ray of 100 W (AlKα anode), the hemispherical analyzer operating in the main fixed analyzer transmission mode, entrance slit of 7 × 20 mm and exit slit open with mesh. The data were recorded with a PHOIBOS 150 NAP 1D-DLD and the total pressure in the main vacuum chamber during analysis was around 5 10^{-9} mbar. Survey spectrum was collected at 80 eV of pass energy and 0.7 eV of step size. To obtain more detailed information about chemical environment and oxidation states, high-resolution spectra were recorded from individual peaks at 30 eV of pass energy, 0.3 Dwell Time and 0.05 eV of step. Due to the poor conductivity of the samples, a flood gun source (COSCON − FG 22/35, SPECS) had to be used to compensate for charging problems and the size of the X-ray spot had to be increased. To characterize the reduced catalysts, the samples were reduced previously in a high-pressure cell (HPC) connected to the main chamber through the load lock chamber. The reduction was carried with a flowrate of 10 mL_n·min^{-1} of hydrogen (99.999 % purity) at 600 °C and 1 bar during 1 h (heating ramp 10 °C·min^{-1}). After the reduction, the hydrogen was evacuated until the pressure in the HPC chamber was lower than 8·10^{-8} mbar. Afterwards, the samples were transferred to the main chamber in UHV conditions, thus preventing the samples from coming into contact with air. Each specimen was analyzed at an emission angle of 0° as measured from the surface normal. Data processing was performed using CasaXPS processing software (version 2.3.26.PR1.0, Casa Software Ltd., Teignmouth, UK). Binding energies were referenced to the C 1 s peak at 284.8 eV (adventitious carbon) [56]. The atomic concentrations of the detected elements were calculated using integral peak intensities and the sensitivity supplied by the manufacturer. The Ni $2p_{3/2}$ region was fitted following the methodology described by Beisinger [56,57], in which each nickel species is fitted using distinct components. The analysis of the Ce 3d region was carried out following Schierbaum's procedure [58] and Burroughs nomenclature [59]. The rest of elements were fitted using a Gaussian-Lorentzian function.

2.3. Steam reforming procedure and product analysis

The steam reforming activity of the catalysts was studied at atmospheric pressure on a laboratory-scale continuous packed bed reactor. A description of the unit and a schematic diagram are provided in the supplementary material (Fig. S1). Experiments were conducted with ca. 250 mg of calcined catalyst sieved to 200 – 300 μm. To improve temperature homogeneity in the packed bed, the catalysts were diluted with ca. 6 g of quartz particles of the same granulometry. Prior to the reaction, the precursors were reduced in situ with 10 mL_n·min^{-1} of hydrogen by heating at 10 °C·min^{-1} from room temperature to 600 °C and keeping that temperature for 18 h. After reduction, temperature was adjusted to the reaction value, the flow of hydrogen was interrupted, 50 mL_n·min^{-1} of nitrogen were added to the system as internal standard for the chromatographic analysis of the product gas, and the feed of the aqueous solution of levulinic acid was started. Typically, a flowrate of 0.2 mL·min^{-1} delivered by a Gilson 305 HPLC pump was used, but the actual mass flowrate of liquid fed during each test was calculated by recording the variation of the mass in the feed reservoir with a balance. Each catalyst sample was tested for a time on stream of 16 h under constant conditions. After the reactor, the product was cooled to 5 °C in a gas–liquid separator. The liquid consisted of water, unconverted levulinic acid and trace amounts of byproducts. It was collected in separate fractions every 2 h and the mass of each fraction was measured with a scale. The concentration of unconverted levulinic acid in each sample was determined by HPLC on an Agilent 1100 chromatograph equipped with a refractive index detector and an Aminex HPX 87-H column (Bio-Rad) at 55 °C. A flowrate of 0.6 mL·min^{-1} of a 0.005 mol·L^{-1} H_2SO_4 aqueous solution was used as solvent. The detector was calibrated with standards of known mass fractions of levulinic acid in deionized water. Samples of the liquid phase were extracted with $CHCl_3$ to isolate unknown compounds appearing in the HPLC analysis. Identification of the main compounds in the extract was performed by nuclear Magnetic Resonance (NMR) in a Bruker Avance Neo 400 MHz spectrometer. ^1H NMR (401 MHz) and ^{13}C NMR (101 MHz) spectra were obtained as solutions in deuterated chloroform. Chemical shifts were reported in parts per million (ppm, δ). For 1H NMR spectra, multiplicities were reported as s (singlet), d (doublet), t (triplet), q (quartet), m (multiplet) or a combination of these. The composition of the dry gas was determined with an online gas chromatograph (3000 microGC system, Agilent Technologies). Gas samples were automatically analyzed along the activity test every 5 min. The products observed in the gas were hydrogen, methane, carbon dioxide, carbon monoxide, and trace amounts of ethane and ethylene. The molar flow rates of the gas products (F_j) were calculated from the molar flowrate of nitrogen added to the reactor as internal standard during the test ($F_{N2,0}$), and the molar fraction composition of the dry gas (x_j), averaged during the 2 h period of collection of a liquid sample (equation (1). The fractional conversion of levulinic acid (X_{LA}), the selectivity to hydrogen (S_{H2}) and to carbon-containing products (S_j), the fractional yield of hydrogen (Y_{H2}), and the carbon balance closure (CB) were calculated according to equations (2) to (6), where $F_{LA,0}$ is the feed molar flow rate of levulinic acid, F_j is the molar flow rate of species j at the reactor outlet, and n_{Cj} is the number of carbon atoms in species j.

$$F_j = F_{N2,0}\left(\frac{x_j}{x_{N2}}\right) \text{ with } j = CO_2, CO, CH_4, C_2H_6, C_2H_4, H_2 \quad (1)$$

$$X_{LA} = \frac{F_{LA,0} - F_{LA}}{F_{LA,0}} \quad (2)$$

$$S_{H2} = \frac{F_{H2}}{11\left(F_{LA,0} - F_{LA}\right)} \quad (3)$$

$$S_j = \frac{n_{C_j} F_j}{5\left(F_{LA,0} - F_{LA}\right)} \text{ with } j = CO_2, CO, CH_4, C_2H_6, C_2H_4, AGL \quad (4)$$

$$Y_{H2} = \frac{F_{H2}}{11\,F_{LA,0}} \quad (5)$$

$$CB = \frac{1}{5\,F_{LA,0}} \sum_j n_{C_j} F_j \text{ with } j = LA,\ CO_2, CO,\ CH_4, C_2H_6,\ C_2H_4, AGL \quad (6)$$

When an activity test concluded, the reactor was cooled to room temperature under a constant flow of 10 $mL_n \cdot min^{-1}$ of nitrogen and the bed material was recovered. The catalyst was separated from the silica particles using a magnet and it was stored in sealed vials for further analysis. The used catalysts were labeled adding the suffix *−Um* to their tags, where *m* represented the S/C ratio of the experiment (for instance: HT450/Ce4-U8.4).

2.4. Reaction conditions

The steam reforming experiments were performed at 500 and 600 °C using steam-to-carbon molar ratios S/C of 2.4, 5.4 and 8.4, which correspond to mass fraction compositions of levulinic acid (LA) in water of 0.349, 0.189 and 0.131. Temperature was limited to 600 °C to avoid surpassing the Tammann temperature of nickel and prevent catalyst sintering [46]. Concerning the S/C ratio, a minimum of 2.4 was chosen to ensure that thermodynamically stable carbon could not form in the system. For a specific organic feed, temperature, and pressure, stable carbon deposits will form below a critical steam-to-carbon ratio [60,61] that is determined by thermodynamics, even if carbon deposits typically occur above this thermodynamic S/C limit due to the reaction mechanisms involved in steam reforming. Even if catalyst coking is kinetically controlled [62,63], conditions that favor thermodynamically stable carbon deposits during the reaction should always be avoided. The conditions that lead to stable carbon during the steam reforming of LA were assessed to select S/C ratios that were suitable for the catalytic activity tests. The combinations of temperature and S/C that led to the formation of stable solid carbon were calculated at absolute pressures of 1, 10 and 30 bar. Calculations were performed with the ASPEN Plus v12 process simulator using the PSRK (Predictive Redlich-Kwong-Soave) thermodynamic method, based on the minimization of the free energy of the system at the specified temperature, pressure, and feed composition (Gibbs reactor). The minimum S/C ratio required to prevent stable carbon decreased with temperature (Fig. 1). Pressure had little influence on the carbon formation boundary between 250 and 600 °C and favored the formation of stable carbon above that temperature. Below 250 °C, the boundary became independent of the S/C ratio once temperature was low enough to form a liquid phase by the condensation of water. At the pressures considered, an S/C ratio above 1.6 was needed to prevent stable carbon at 500 °C. This S/C ratio is higher than the stoichiometric requirement of 1.4 needed to completely convert levulinic acid ($C_5H_8O_3$) to carbon dioxide and hydrogen (equation (7), and it justifies the use of an excess of steam to conduct the reaction. A minimum S/C of 2.4, which is ca. 50 % above the thermodynamic limit between 500 and 600 °C was therefore chosen. Still, the steam reforming of oxygen-containing compounds and hydrocarbons larger than methane involves a complex set of reactions that is represented poorly by the general stoichiometry in equation (7). A better description is given considering the water gas shift and the methanation reactions as well (equations (8) to (10). An excess of water is not only needed to prevent stable carbon, but to minimize the formation of carbon monoxide and methane by displacing the water shift and methanation reactions towards the formation of hydrogen and carbon dioxide. This is illustrated in Fig. 1, where the equilibrium yield of hydrogen and the selectivity to methane and carbon oxides are depicted at atmospheric pressure for S/C ratios of 2.4, 5.4 and 8.4. The equilibrium yield of hydrogen in the 500 – 600 °C region chosen for the experiments is very sensible to the S/C ratio since CH_4 and CO are favored at low S/C. Based on those results, S/C ratios of 2.4, 5.4 and 8.4 were selected to conduct the catalyst screening

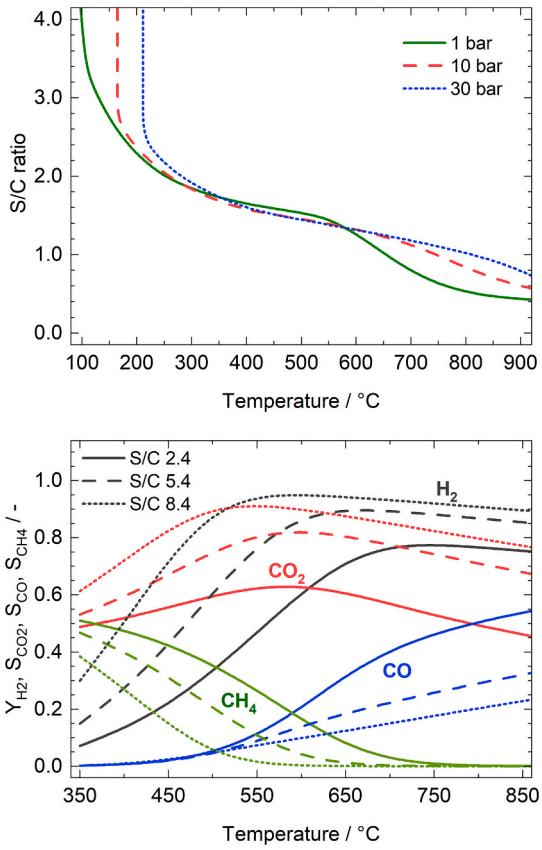


Fig. 1. Thermodynamic analysis of the steam reforming of levulinic acid: temperature – S/C boundaries for the formation of stable carbon deposits at absolute pressures of 1, 10 and 30 bar (top), and equilibrium yield of hydrogen and selectivity to methane and carbon oxides in dry-basis at atmospheric pressure and S/C ratios of 2.4, 5.4, and 8.4 (bottom).

experiments. These values fall within the range of 1.5 to 24 used in the available literature for the SR of LA [54,55].

$$C_xH_yO_z + (2x - z)H_2O \rightarrow xCO_2 + \left(2x + \frac{y}{2} - z\right)H_2 \quad (7)$$

$$C_xH_yO_z + (x - z)H_2O \rightarrow xCO + \left(x + \frac{y}{2} - z\right)H_2 \quad (8)$$

$$CO + H_2O \rightleftarrows CO_2 + H_2 \quad (9)$$

$$CO + 3H_2 \rightleftarrows CH_4 + H_2O \quad (10)$$

3. Results and discussion

3.1. Catalyst characterization

Composition of the calcined materials was determined by FESEM (Table 1). A nickel atomic ratio from 40 to 50 % was obtained with ratios between bivalent and trivalent metals (M^{2+}/M^{3+}) close to 3, the typical value in naturally existing hydrotalcites. In the promoted catalysts, the Zr content was found to be from 0.77 to 0.95 atomic %, while Ce was 0.40 %. Nitrogen physisorption was used to determine the textural properties of the calcined materials. All had type IV isotherms with type H4 hysteresis loops according to the IUPAC classification (Fig. S2), which are characteristic of materials formed by parallel laminar structures [64]. The surface area of the material calcined at 450 °C (HT450) was only 60 $m^2 \cdot g^{-1}$, with a pore volume of 0.27 $mL \cdot g^{-1}$ and an average diameter of 8.4 nm (Table 1 and Fig. S2). Calcination at 600 °C (HT600) gave a surface area of 102 $m^2 \cdot g^{-1}$ with a pore diameter of 7.1 nm, but at

Table 1
Characterization of the calcined materials: textural properties determined from the nitrogen adsorption isotherms, and metal elemental composition based on FESEM surface analysis.

	Textural properties			Elemental analysis					
Catalyst	S_{BET} ($m^2 \cdot g^{-1}$)	V_{BJH} ($mL \cdot g^{-1}$)	d_{BJH} (nm)	Ni (wt%)	M^{2+}/M^{3+}	Ni (atom %)	Mg (atom %)	Al (atom %)	X (atom %)
HT450	60	0.27	8.4	39.2	2.6	43.4	28.7	27.9	–
HT600	102	0.37	7.1	48.1	2.8	50.3	23.4	26.3	–
HT750	69	0.54	17.4	46.6	2.9	48.2	25.9	25.9	–
HT450/Zr	88	0.35	8.4	42.8	3.0	46.6	27.8	24.8	0.8
HT600/Zr	88	0.51	9.9	38.8	3.1	47.9	27.2	24.0	0.9
HT750/Zr	87	0.50	11.9	43.8	3.1	47.8	27.0	24.2	1.0
HT450/Ce4	112	0.41	8.3	45.7	3.1	49.5	25.5	24.6	0.4

750 °C (HT750) the pore diameter grew to 17.4 nm with the subsequent decrease in surface area. The addition of zirconia as promoter stabilized the structure of the mixed oxides; surface areas of ca. 88 $m^2 \cdot g^{-1}$ were obtained regardless of the calcination temperature, although pore diameter grew from 8.4 nm in HT450/Zr to 11.9 in HT750/Zr. The addition of ceria to the material calcined at 450 °C (HT450/Ce4) almost doubled the surface area (112 $m^2 \cdot g^{-1}$) of the unpromoted HT450 without changing the average pore diameter.

The unpromoted and Zr-promoted coprecipitated precursors presented the XRD diffraction signals characteristic of a layered double hydroxide phase with a hydrotalcite-like structure (Fig. S3). No other phases were observed, which indicates the isomorphic replacement of Mg^{2+} cations by Ni^{2+} and Al^{3+} in the brucite layers. On both precursors, there was a superposition of planes (009) and (012) around 34.9 degrees that is characteristic of hydrotalcites with a high degree of purity [65]. The XRD patterns of the calcined samples (Fig. 2) had reflections characteristic of oxides with a cubic NaCl-type crystal structure (s.g. Fm3m) typical NiO (PDF#00–047-1049, a = 4.177 Å), formed by decomposition of the hydrotalcite above 300 °C [66–69]. The diffraction peaks at 37.4, 43.7, 63.3, 76.1, and 79.6 corresponded to planes (111), (200), (220), (311), and (222), respectively. The intense (111) reflection was related to an enrichment in Ni cations in the mixed oxides [67]. The crystallinity of this phase was similar after calcination at 450 and 600 °C, but it grew in the sample calcined at 750 °C (HT750). Promotion with Zr gave a similar crystallinity regardless of the calcination temperature. Finally, the sample promoted with ceria (HT450/Ce4) presented a peak with low crystallinity at 28.6 degrees of the (111) plane of CeO_2 (fluorite structure, PDF#00–034-0394), which is characteristic of a good impregnation of the precursor oxide with ceria. In all the calcined materials, signals corresponding to a segregated alumina phase were not observed, which indicates that aluminum was integrated into the crystalline network of mixed oxides [70].

H_2-TPR of the calcined materials (Fig. S4) revealed peaks related to the reduction of nickel oxide to metallic nickel. The catalysts calcinated at 450 °C presented two asymmetric peaks. The first around ca. 350 °C can be assigned to the reduction of nickel oxide and hydroxides with weak interactions with Mg(Al)O, or the reduction of surface oxygen or oxygen capping species. The second peak, located at 540 °C, corresponded to the reduction of the bulk nickel oxide with strong interaction with a MgAl mixed oxide phase [69,71,72]. Calcination temperature suppressed the low interaction peak and shifted the strong interaction peak to higher reduction temperatures due to the formation of a spinel phase. Promotion with Zr had a clear impact on reducibility. In the HT450/Zr material, the presence of Zr increased the amount of nickel oxides with weak interaction with the support, but simultaneously shifted the temperature of the strong interaction oxides from 540 to 646 °C. The shift in the temperature of reduction was even more important in HT600/Zr and especially in HT750/Zr, where the addition of zirconia increased the interaction of the nickel oxide with the mixed oxide matrix and decreased its reducibility. The lower reducibility of NiO in the materials calcined at higher temperature agreed with NiO showing more intense signals in the XRD spectra due to a higher crystallinity and stronger interaction with the support. Concerning the

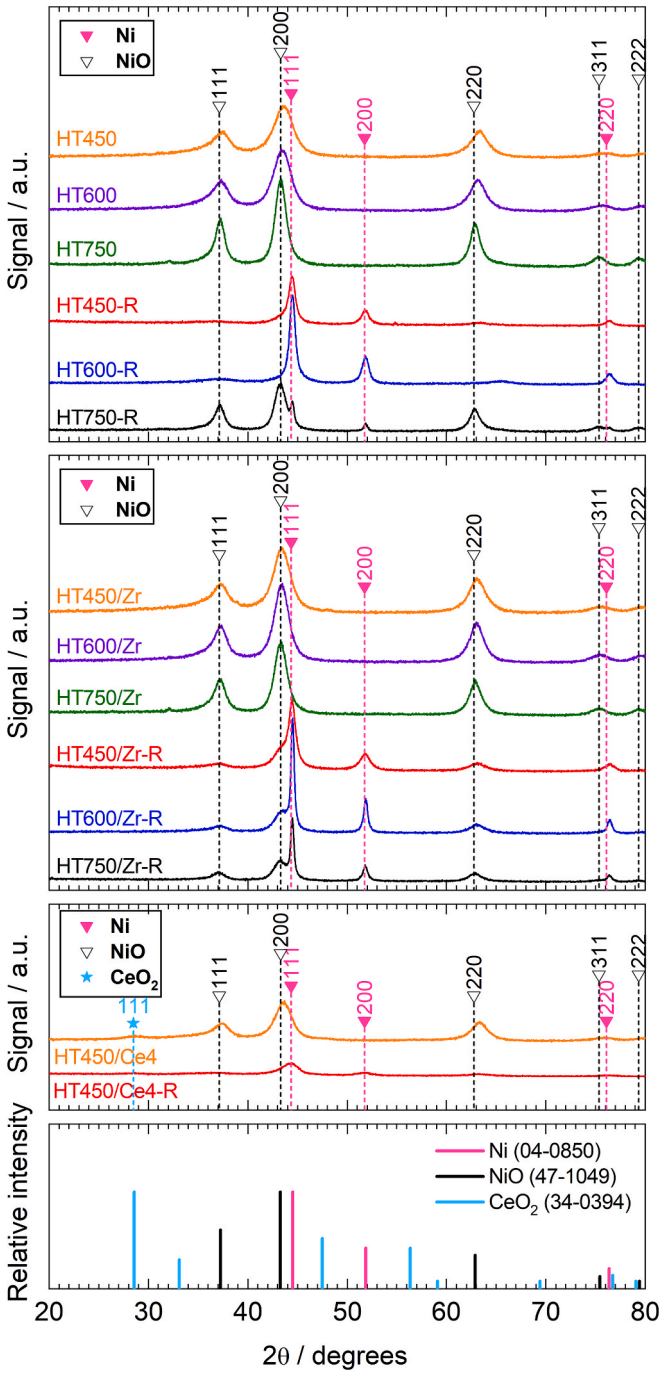


Fig. 2. XRD diffractograms of the HT samples calcined at 450, 600 and 700 °C, and reduced at 600 °C: unpromoted (top), promoted with Zr (center), and HT450 promoted with Ce (bottom).

promotion with Ce, only a small displacement in the reduction temperature was observed compared to the unpromoted HT450.

The XRD spectra of the HT450-R catalyst reduced at 600 °C (Fig. 2) revealed a crystalline phase of metallic nickel with peaks at 44.9, 51.7 and 76.3 degrees with a cubic unit cell parameter a = b = c = 3.525 Å (PDF#00–004-0850, a = b = c = 3.524 Å). The diffractogram also contained very weak signals characteristic of NiO with cubic NaCl-type crystal structure (PDF#00–047-1049). The small contribution of the NiO signals in HT450-R suggests that a high degree of nickel reduction at 600 °C, in agreement with H_2-TPD, and a high dispersion and small crystallite size of the unreduced NiO. The precursor calcined at 600 °C also showed weak signals of NiO and intense signals of Ni^0, pointing to the formation of larger crystallites of reduced nickel. In HT750-R, however, reduction at 600 °C was clearly incomplete since the diffraction bands of Ni^0 were noticeably smaller than those of NiO. Reduction of the Zr-promoted materials was incomplete regardless of the calcination temperature, and even in HT450/Zr-R the signals of the NiO planes were well defined. This was consistent with the lower reducibility of these materials as determined from H_2-TPR. Finally, the ceria-promoted catalyst, HT450/Ce4-R, only presented small signals of Ni^0 with weak contributions of NiO and CeO_2. The sizes of the reduced nickel particles were calculated from the XRD diffractograms and they were also determined from HR-TEM imaging of the reduced catalysts for the materials obtained by calcination at 450 °C (Table 2 and Fig. S5. More detailed HR-TEM/EDX images of the three reduced catalysts are presented in Fig. S6, S7 and S8). Both methods gave equivalent results. The addition of CeO_2 as promoter improved the dispersion of Ni^0 and reduced the average nickel crystallite size from ca. 17.8 nm in the unpromoted HT450-R to 8.5 nm in HT450/Ce4-R. On the contrary, the addition of Zr aggregated nickel in larger crystallites with an average diameter of ca. 25 nm and a broad distribution of sizes because of the stronger interaction with the support (Fig. S5). This agrees with the higher reduction temperatures of the materials promoted with zirconia. HR-TEM/EDX also revealed a complete dispersion of Zr and Ce in the promoted catalysts (Fig. S7 and S8, respectively).

The chemical states of the surface components of HT450-R, HT450/Zr-R and HT450/Ce4-R were studied by XPS (Fig. 3). The samples were reduced in situ prior to the analysis to avoid the reoxidation of nickel upon contact with air. The O 1 s spectra of the three catalysts presented a dominant peak centered at low binding energy (530 – 531 eV) corresponding to lattice oxygens (O_L), and a small shoulder at high binding energy (532 – 533 eV) related to oxygen vacancies in superficial defects of the lattice structure (O_V) [39,41]. The defects on the lattice facilitate the adsorption of water and its mobility during steam reforming. The ratio between oxygen vacancies and lattice oxygen (O_V/O_L) was 0.25 in HT450-R, 0.23 in HT450/Ce4-R and 0.22 in HT450/Zr-R. At the amounts used in this study the addition of Ce and Zr did not create additional lattice defects, and it even decreased their concentration slightly. The Ni $2p_{3/2}$ spectra were fitted following the procedure described by Beisinger [56,57] and the proportion of reduced nickel (Ni^0) was calculated from the areas of the Ni^0 and Ni^{2+} peaks. The percentage of Ni^0 was 36.3 % in HT450-R, 48.2 % in HT450/Ce4-R and 51.1 % in HT450/Zr-R. The addition of Zr augmented the presence of nickel oxides with low reducing temperature (Fig. S4) and formed larger Ni^0 particles (Table 2), which resulted on a larger fraction of reduced nickel surface. Concerning Ce in HT450Ce4-R, it interacted with nickel favoring its dispersion and improving its reducibility. The Ce 3d XPS spectra was analyzed following Schierbaum's procedure [58]. The $Ce^{3+}/(Ce^{3+} + Ce^{4+})$ ratio was 58.2 %. Since Ce was used as a dopant agent, it was dispersed through the surface in the vicinity of the particles of reduced nickel. Ce^{3+} thus created oxygen vacancies on the vicinity of the nickel particles, even if the total number of vacancies was close to that of the unpromoted catalyst due to the predominant presence of oxygen in aluminum and magnesium mixed oxides.

Temperature programmed desorption of carbon dioxide (CO_2-TPD) was used to determine the basicity of the reduced catalysts (Table 2 and

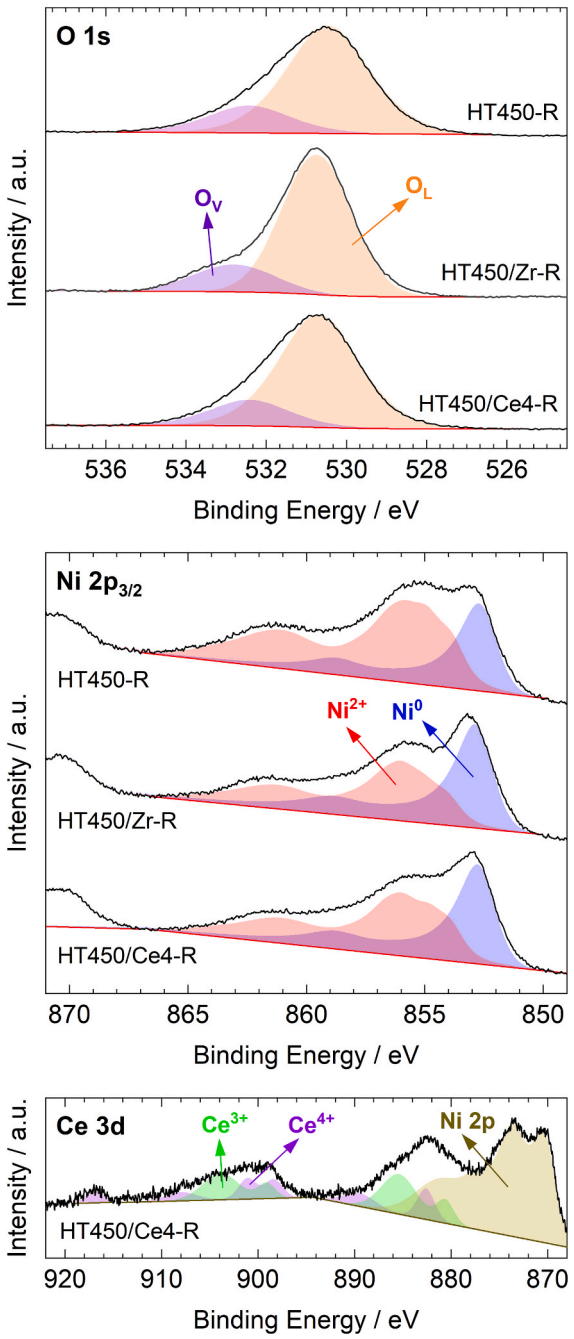


Fig. 3. XPS spectra of the reduced catalysts: O 1 s (top), Ni $2p_{3/2}$ (middle), and Ce 3d (bottom).

Table 2
Characterization of the reduced catalysts. Average Ni particle diameters determined by XRD and HR-TEM, and distribution of basic sites determined by CO_2-TPD.

Catalyst	Average diameter (nm)		Basic sites (mmol $CO_2 \cdot g^{-1}$)			
	HR-TEM	XRD	Total	Weak	Middle	Strong
HT450-R	14.7	17.8	0.340	0.053	0.216	0.071
HT600-R	–	20.3	0.230	0.035	0.122	0.074
HT750-R	–	36.8	0.242	0.032	0.127	0.071
HT450/Zr-R	27.1	25.5	0.401	0.071	0.213	0.116
HT600/Zr-R	–	25.2	0.313	0.104	0.117	0.092
HT750/Zr-R	–	28.7	0.274	0.093	0.099	0.081
HT450/Ce4-R	8.2	8.5	0.306	0.077	0.171	0.058

Fig. S9), which in this type of materials is highly dependent on the composition and the use of promoters [71,73–75]. The signals were deconvoluted as the superposition of three peaks corresponding to the desorption of CO_2 from weak basic sites associated with Brønsted OH groups (100 to 150 °C), the desorption of CO_2 from bidentate carbonates on intermediate strength metal–oxygen Lewis pairs (170 to 220 °C), and the release of CO_2 attached to oxygen anions in strong Lewis sites (> 250 °C) [72,76–78]. Catalyst HT450-R had a total basicity of 0.340 mmol $CO_2 \cdot g^{-1}$ with a predominance of middle-strength Lewis sites. Calcination temperature decreased the total basicity and tended to reduce weak and intermediate sites while strong Lewis sites remained constant. Addition of Zr increased the total basicity of the catalysts. Weak and strong sites increased, while those of intermediate strength remained unaffected. Finally, promotion with Ce reduced intermediate and strong sites (HT450/Ce4-R), while the weak Brønsted groups increased respect the unpromoted catalyst calcined at the same temperature. Similar effects have been reported in literature for nickel-based catalysts supported on Ce and Zr oxides [71,72].

3.2. Catalytic activity

3.2.1. Unpromoted catalysts

The unpromoted catalysts were tested under constant conditions for a time on stream of ca. 16 h. The activity test of catalyst HT450 at 500 °C and an S/C ratio of 8.4 illustrates a typical experiment (Fig. 4). The fractional conversion of LA was complete at the beginning of the run, but it decreased until it stabilized at ca. 0.80 ± 0.02 after 8 h. The yield of hydrogen and the selectivity to carbon dioxide, carbon monoxide and methane grew from the start and stabilized after 8 h at respective values of 0.68 ± 0.03, 0.73 ± 0.02, 0.070 ± 0.003 and 0.049 ± 0.006. The carbon balance followed the same trend. It was only 0.79 after 2 h of time on stream, and it grew to an average value of 0.96 ± 0.06 beyond 8 h. The unsteady behavior during the initial stage of the experiment was caused by two factors. First, the dead volume of the system (feed and product lines, reactor, condenser and gas liquid separator), which was initially filled with nitrogen gas and had to be flushed by the reformate gas. From blank experiments at low temperature with only silica particles in the bed, it was determined that the time needed to reach a steady state in the composition of the gas and the liquid products was less than one hour. The second factor was related to the stabilization of the fresh catalyst. The dry reformate gas composition measured by the online microGC every 5 min (Fig. 4) showed that it took more than 4 h to stabilize the composition of the reformate gas. The gas had lower concentrations of hydrogen and carbon dioxide and more carbon monoxide at the beginning of the run, especially during the first two hours. Ethylene and ethane were the only higher hydrocarbons present, and only in trace amounts. They reached maximum molar fractions of ca. 1.3 10^{-3} and 5.0 10^{-4} after only 30 min of experiment and decreased afterwards. Ethylene is a well-known precursor of carbon deposition on nickel-based catalysts, and its presence in the reformate gas is a signal of catalyst coking. An unknown byproduct was observed as well in the HPLC chromatograms of the samples of liquid (Fig. S10). After extraction with chloroform and analysis by NMR it was identified as β-angelica lactone (AGL, Fig. S11). The selectivity to AGL reached a maximum of 0.045 after 4 h and stabilized at 0.032 ± 0.003 after 10 h. The reaction pathways of LA leading to the identified products are presented in Scheme 1, which is based on the stablished mechanisms involved on the steam reforming of higher hydrocarbons and oxygenated molecules [60–63,79–81]. It is proposed that LA decomposes by α-scission of the carbon–carbon bonds to form reactive CH_n species, carbon, and carbon monoxide absorbed on the catalyst. Those may react on the nickel crystallites with water adsorbed on the superficial oxygens of the lattice of metal oxides of the support to produce hydrogen and carbon dioxide by the steam reforming and the water gas shift (WGS) reactions. Alternatively, the adsorbed carbon species can diffuse into the nickel crystallites to form carbon filaments by nucleation, or they may form

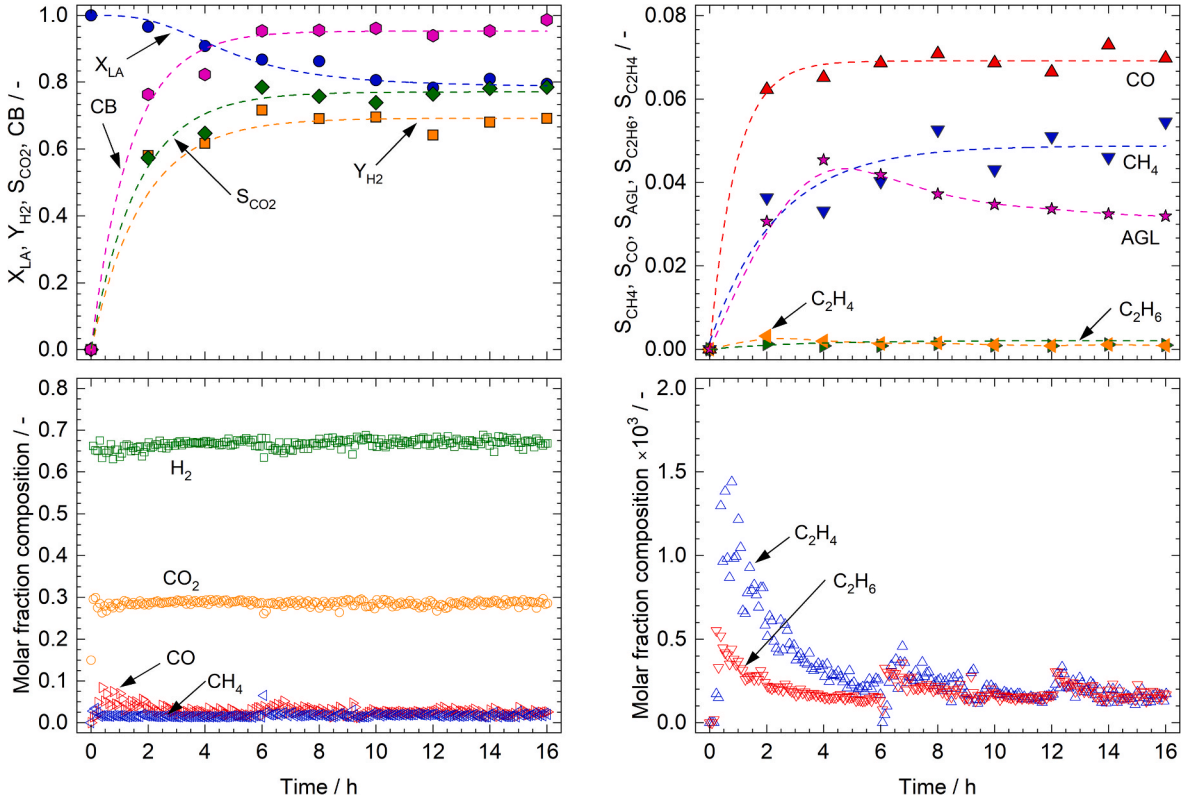
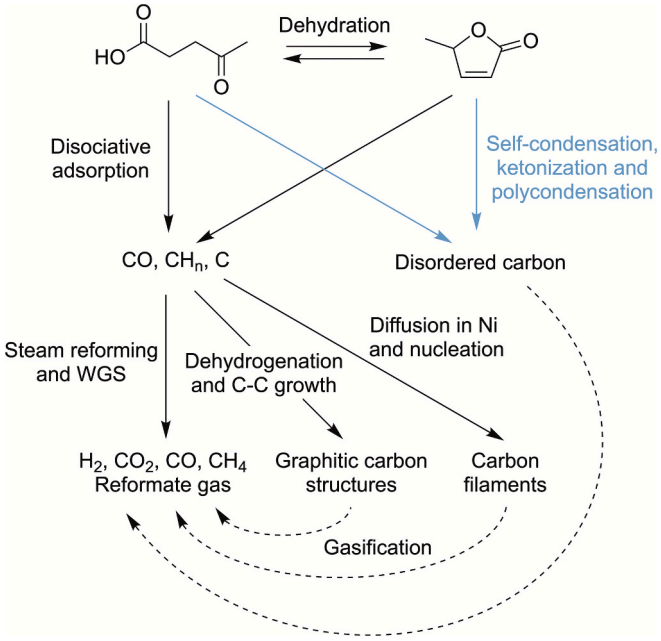


Fig. 4. Catalytic activity test of HT450-R at atmospheric pressure, 500 °C, and an S/C ratio of 8.4 (S/C of 8.4). Top: levulinic acid conversion, hydrogen yield, carbon balance, and selectivity to the identified products. Bottom: molar fraction composition of the dry-gas. The dashed lines only visualize trends.



Scheme 1. Reaction pathways occurring in the steam reforming of levulinic acid.

encapsulating graphitic carbon structures by dehydrogenation, surface migration and growth. Cracking is responsible for the formation of ethylene, which may detach from the catalyst surface, be hydrogenated to ethane, or evolve into carbon deposits by polymerization. Concerning AGL, it is formed by the dehydration of LA on acidic or basic sites, which is an endothermic and reversible reaction. The partial pressure equilibrium constant of this reaction was estimated to be of only 0.2 atm at 275 °C from experimental data [82]. The equilibrium constant should be higher at the usual steam reforming temperatures, but the formation of AGL would be hindered by the large excess of water used in the process (H_2O/LA molar ratios of 12, 27 and 42 in our case), which is consistent with the low selectivity to AGL that we have observed. In addition, above 300 °C AGL undergoes oligomerization and cracking to form amorphous carbon deposits [82]. Likewise, LA may react on acidic and basic surfaces by self-condensation [83,84] and may undergo ketonization and polycondensation [85–88], leading to the formation of disordered carbonaceous deposits at high temperature.

The effect of the steam-to-carbon molar ratio (S/C) was explored with the HT450 catalyst at a reforming temperature of 600 °C using S/C ratios of 2.4, 5.4 and 8.4 (Fig. 5). The reported results correspond to the average values and their uncertainties at the 95 % probability level determined from the data gathered after the catalyst achieved near-stationary conditions. An experiment performed with an inert bed of silicon dioxide at 600 °C and a S/C of 8.4 proved that the decomposition of levulinic acid by the combination of homogeneous thermal reactions and an eventual catalytic action of the reactor's stainless-steel walls or the particles of SiO_2 was not extensive. Fractional conversion was below 0.1 and the only gas products detected were hydrogen and carbon dioxide. The carbon balance was 0.97 ± 0.02, which falls within the expected results in steam reforming studies. The silicon dioxide particles recovered after the test were light gray in color. The eventual gain in the mass of the bed material caused by the accumulation of carbon was negligible, even if it could not be measured accurately due to the practical impossibility of recovering all the silicon particles loaded into the reactor. With the HT450 catalyst the conversion of LA was complete (> 0.9995) at the three S/C ratios studied. A larger excess of steam favored the yield of hydrogen and the selectivity to carbon dioxide over methane and carbon monoxide. However, the yield of hydrogen and the selectivity to carbon oxides were lower than those corresponding to

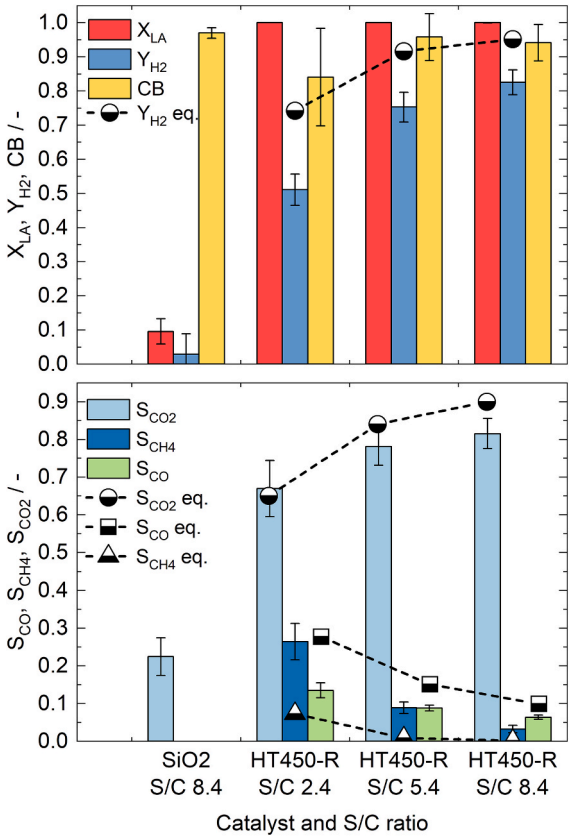


Fig. 5. Catalytic activity tests of HT450-R at atmospheric pressure, 600 °C, and 4/C ratios of 2.4, 5.4 and 8.4. Top: levulinic acid conversion, hydrogen yield and carbon balance. Bottom: selectivity to carbon dioxide, methane, and carbon monoxide. The dashed lines only visualize trends of the equilibrium values.

equilibrium at 600 °C while the selectivity to methane was higher. The carbon balances were acceptable except at an S/C of 2.4, where it was only 0.84 ± 0.14. The poor balance and the large dispersion were caused by the deposition of carbon on the packed bed, which led to a partial blockage and an irregular flow through the system due the rise of the reactor pressure. At a S/C ratio of 2.4 the availability of adsorbed water was insufficient to make steam reforming, WGS, and carbon gasification faster than the processes leading to carbon deposition. Furthermore, the low concentration of water facilitated the formation of AGL by dehydration of LA. The condensation reactions of AGL and LA and the growth of carbon filaments were probably dominant given the rapid accumulation of carbon and the partial bed blockage. At higher S/C ratios, superficial water made SR faster, which reduced coking by filament growth and encapsulation, impeded the formation of AGL, and facilitated a faster gasification of the of disordered and more reactive carbon originated from LA and AGL, but it promoted the sintering of nickel. Sintering and partial reoxidation due to the action of steam were observed on the spent catalysts at the three S/C ratios by XRD (Fig. 6). The materials displayed small diffraction signals of NiO, which were absent on HT450-R, and had signals of Ni^0 stronger than those of HT450-R indicating larger crystallite sizes. The extent of sintering grew with the S/C ratio. A wide diffraction signal at 26° corresponding to graphitic carbon was observed, especially in the test at a S/C ratio of 8.4, which is consistent with the formation of more carbon filaments due to the increase in the size of the nickel crystallites by sintering.

The temperature of calcination influenced the crystallinity of the mixed oxide precursors and their reducibility, as it was previously discussed. The reforming activity of the unpromoted catalyst calcined at different temperatures and reduced at 600 °C was tested at an S/C of 8.4 and 500 °C (Fig. 7). Conversion of LA was 0.81 in HT450-R with a

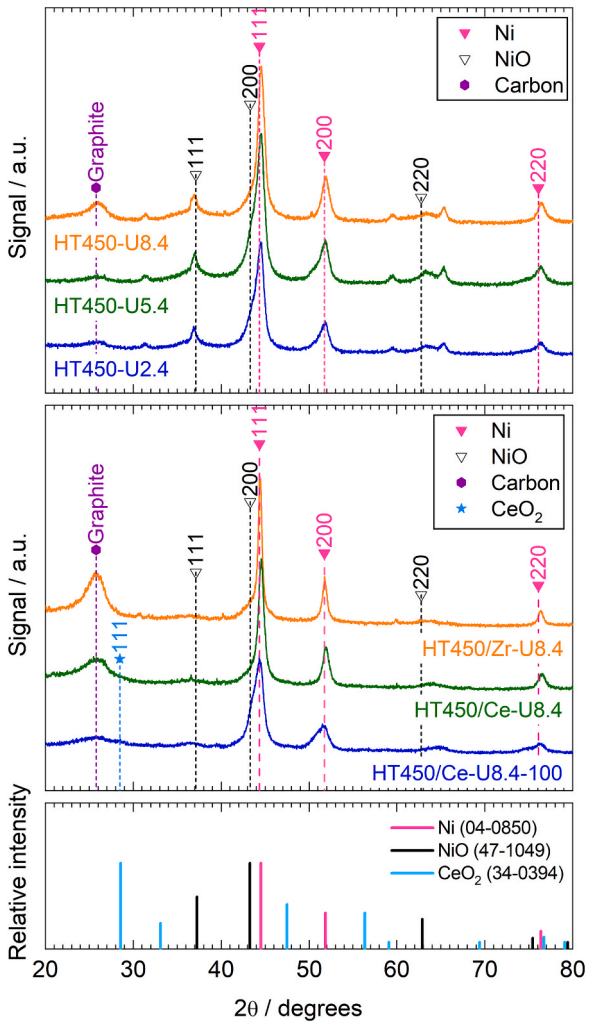


Fig. 6. XRD diffractograms of the used catalysts. Top: unpromoted HT450-R catalyst after reaction at 600 °C and S/C ratios of 2.4, 5.4 and 8.4 (HT450-U2.4, HT450-U5.4 and HT450-U8.4). Bottom: promoted catalysts after reaction at an S/C ratio of 8.4 and 500 °C (HT450/Zr-U8.4 and HT450/Ce4-U8.4), and the HT450/Ce4-R tested for 100 h at S/C of 8.4 and 600 °C (HT450/Ce4-U8.4–100).

hydrogen fractional yield of 0.68 and a carbon balance of 0.96. Selectivity to carbon dioxide, methane, carbon monoxide and AGL were 0.77, 0.050, 0.060 and 0.034, respectively. The selectivity to ethylene was the highest during the first hour of reaction (3.16 10^{-3}) but stabilized afterwards at 1.10 10^{-3}. The HT600-R catalyst gave better conversion (0.97) and had a similar carbon balance (0.96), but the hydrogen yield and the selectivity to carbon oxides and AGL were lower than those of HT450-R. This was because HT600-R favored methane, with a selectivity of 0.22. This was attributed to a reduced water adsorption capacity of the surface due to the lower amount of weak basic sites in this catalyst (Table 2). Finally, the catalyst calcined at 750 °C had low reforming activity. It had a conversion of 0.80, but the carbon balance was only 0.75 due to an extensive deposition of carbon on the catalyst. This resulted on a low yield of hydrogen and low selectivity to carbon dioxide. The selectivity to ethylene was also very small despite the extent of carbon deposition, and more AGL was formed pointing to a slightly higher capacity for the dehydration of LA. This was consistent with the low presence of weak basic sites to promote water adsorption and the incomplete reduction of Ni in this catalyst, which gave a low density of sites active for reforming and favored coke formation by polymerization of levulinic and its decomposition. Overall, the catalyst prepared from the mixed oxides calcined at 450 °C offered the best results in terms of hydrogen yield and carbon conversion to carbon dioxide.

3.2.2. *Promoted catalysts*

Promotion of the catalysts with Zr and Ce was investigated. The catalysts promoted with Zr were prepared by calcination at 450, 600 and 750 °C and reduction at 600 °C, and their activity was tested at 500 °C with an S/C of 8.4 (Fig. 8). HT450/Zr-R achieved complete conversion of LA with a hydrogen yield and a carbon dioxide selectivity equivalent to those of the unpromoted HT450-R, while the carbon balance was only 0.92 ± 0.04. Selectivity to methane was higher and selectivity to carbon monoxide lower than in the unpromoted catalyst, while AGL was only detected in trace amounts. The calcination temperature had an adverse effect. The conversion of LA, the yield of hydrogen, the selectivity to methane and the carbon balance were lower in HT600/Zr-R and HT750/Zr-R, the selectivity to carbon oxides was mostly unaffected, but the selectivity to ethylene, ethane and AGL increased, especially in HT750/Zr-R. The diffractogram of the spent HT450/Zr-U9 (Fig. 6) exhibited little contribution of a nickel oxide phase and revealed sintering of the metallic nickel phase, that gave stronger signals that in the unused reduced catalyst. This implies that the hydrogen gas formed by the reforming of LA reduced the NiO phase during the activity test, while steam probably induced sintering of the Ni phase. A diffraction band consistent with the graphitic carbon was clearly observed. Promotion

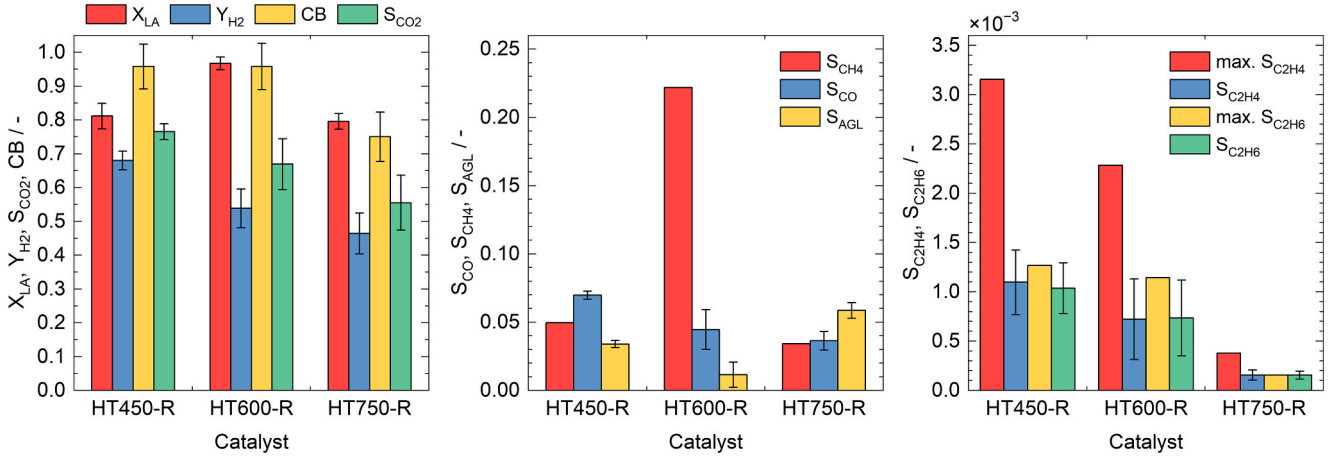


Fig. 7. Catalytic activity test of HT450-R, HT600-R and HT750-R at 500 °C and S/C ratio of 8.4: levulinic acid conversion, hydrogen yield, carbon balance and selectivity to carbon dioxide (left), selectivity to methane, carbon monoxide and β-angelica lactone (center), and selectivity to ethane and ethylene (right).

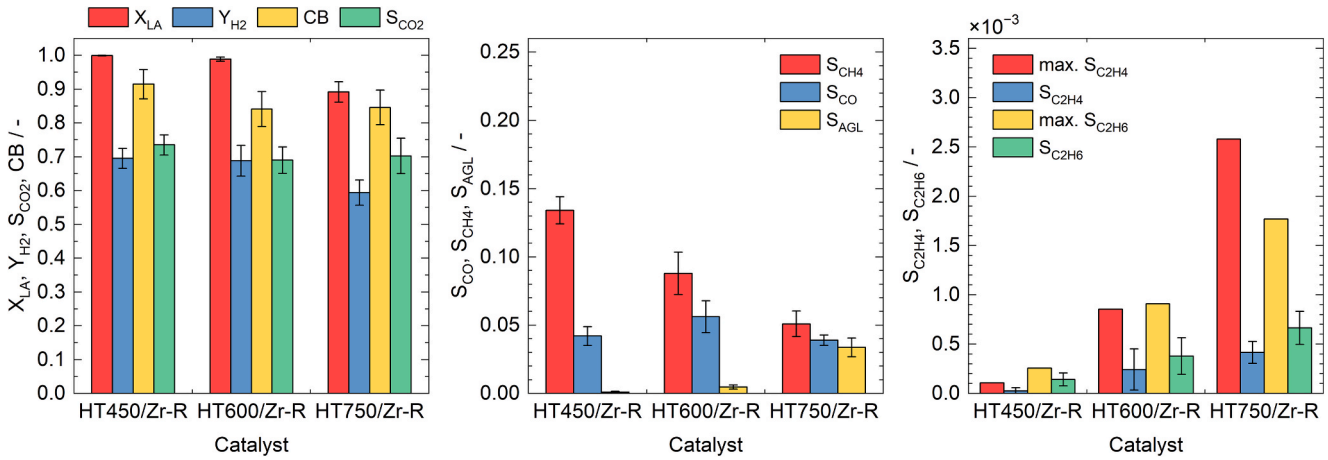


Fig. 8. Catalytic activity test of HT450/Zr-R, HT600/Zr-R and HT750/Zr-R at 500 °C and S/C ratio of 8.4: levulinic acid conversion, hydrogen yield, carbon balance and selectivity to carbon dioxide (left), selectivity to methane, carbon monoxide and β-angelica lactone (center), and selectivity to ethane and ethylene (right).

with Ce was tested by impregnating the HT450 catalyst with 0.12 Ce atom % (HT450/Ce1-R) and 0.40 Ce atom % (HT450/Ce4-R). The activity of both catalysts was measured at 500 °C with an S/C of 8.4 after reduction at 600 °C. To determine the reproducibility of the reaction system and the operational procedure, the catalyst HT450/Ce4-R was tested in duplicate (Fig. 9) giving a LA conversion, a hydrogen yield and a selectivity that were equal in both tests within the uncertainty of the results. The presence of Ce improved the conversion of LA and the yield of hydrogen, and the selectivity to carbon dioxide slightly. The load of Ce did not have a significant effect on the performance of the catalyst, except for a small decrease in selectivity to carbon monoxide, ethane and ethylene, and more methane in HT450/Ce1-R. Overall, the HT450 catalysts promoted with Zr and Ce gave close results, except for the carbon balance that was better in HT450/Ce4-R. Sintering occurred during reforming and the spent HT450/Ce4-U9 presented sharper signals of metallic nickel, as well as a band of carbon, although the latter was more intense in HT450/Zr-U9 (Fig. 6).

The nature of the carbon deposits in the used catalysts (HT450-U9, HT450/Zr-U9 and HT450/Ce4-U9) was investigated by Raman spectroscopy (Fig. S12). The spectra were deconvoluted into the four characteristic bands of coke: the G band at 1600 cm^{-1} caused by condensed, ordered or graphitic aromatic structures, the D (1350 cm^{-1}) and its image D_3 (1500 cm^{-1}) bands corresponding to disordered aromatic structures, and the band at 1200 cm^{-1} resulting from aliphatic C–H bonds [79]. The unpromoted catalyst presented an I_D/I_G intensity ratio of 1.04 indicating the coexistence of disordered and ordered poly-aromatic carbon structures, but also the presence of aliphatic carbon deposits was clear from the band at 1200 cm^{-1}. Promotion with Zr and Ce resulted in carbon deposits that were less aliphatic, and with more disordered aromatic structures (I_D/I_G intensity ratios of 1.22 and 1.21, respectively).

Analysis of the spent catalysts by HR-TEM/EDX gave further evidence of the nature of the deposited carbon. HT450-U9 mostly retained the morphology of the reduced catalyst, but the surface was covered with carbon deposits that also enclosed the nickel crystallites (Fig. 10 and Fig. S13). Nickel particles were present at the growing end of wide carbon whiskers and filaments, but they were covered in carbon as well (Fig. S13). This suggests that carbon deposition during SR of LA evolved following a sequence similar to that proposed by Montero et al. [79] for ethanol SR on a Ni/La_2O_3– α Al_2O_3 catalyst. According to Scheme 1, filamentous aromatic carbon started to grow once CH_n fragments were formed on the fresh catalyst by α −cission of LA. This initial period of ca. 2 h was characterized by little deactivation of the catalyst and the presence of higher concentrations of carbon monoxide and ethylene in the gas (Fig. 4). On a subsequent phase, the catalyst experienced a faster deactivation until it tended to stabilize after 8 h TOS. It is likely that amorphous and disordered aromatic carbon accumulated on the surface by ketonization of LA and condensation of AGL during this period since it corresponded with the maximum concentration of β-angelica lactone on the products. The catalyst then reached a pseudo-steady state in

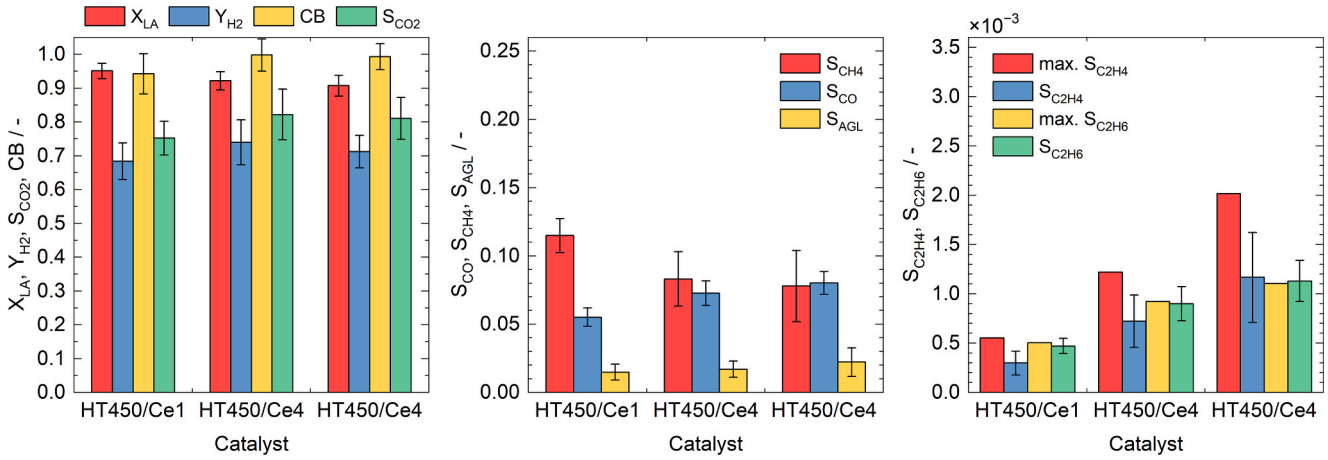


Fig. 9. Catalytic activity test of HT450/Ce1-R and HT450/Ce4-R at 500 °C and S/C ratio of 8.4: levulinic acid conversion, hydrogen yield, carbon balance and selectivity to carbon dioxide(left), selectivity to methane, carbon monoxide and β-angelica lactone (center), and selectivity to ethane and ethylene (right).

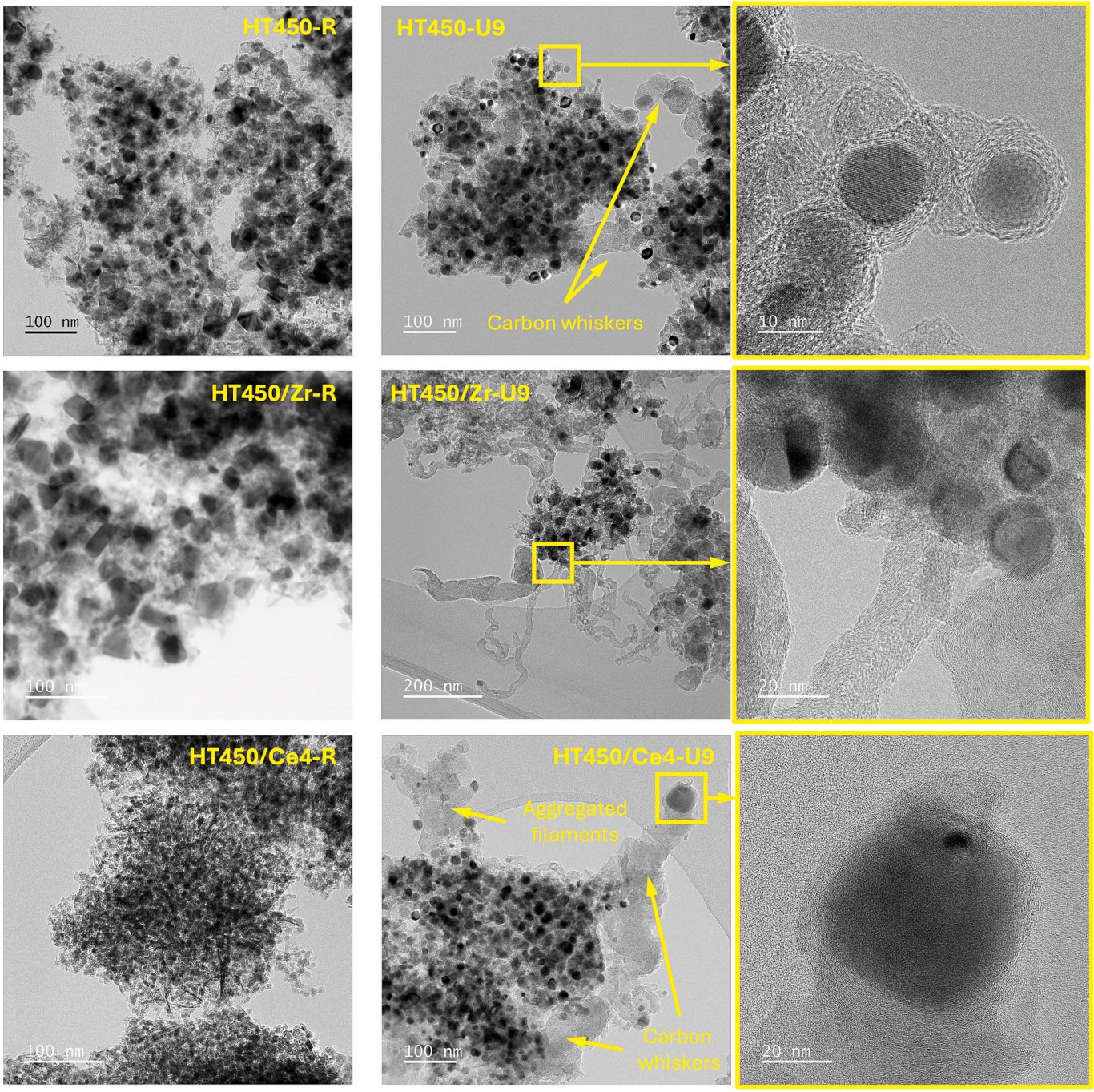


Fig. 10. HR-TEM of the reduced catalysts (left images), and the used catalysts (center and right images) after 16 h of TOS at 500 °C and a S/C ratio of 8.4 (see Fig. S13, S14, S15 and S16 for EDX element mapping).

which the rate of deposition of disordered carbon equilibrated with its rate of gasification, while filamentous carbon and non-filamentous graphitized formations expanded at a lower rate, which allowed the catalyst to maintain its activity during the 16 h of TOS. The addition of zirconium favored the formation of filamentous carbon as the primary coking mechanism on HT450/Zr-U9 (Fig. 10 and Fig. S14). A massive formation of carbon filaments was observed and those disintegrated the catalyst, although most nickel particles remained attached to fragments of the magnesium–aluminum oxide matrix. Furthermore, the layer of disordered carbon covering the surface was absent in most of the sample. This was due to the large size of the nickel crystallites in HT450/Zr-R (27.1 nm, Table 2), which induced the diffusion of carbon into the nickel crystallite and the grow of filaments by nucleation as the preferential route for coking. Concerning HT450/Ce4-U9, it presented sections that maintained the original morphology of the catalyst although the nickel particles appeared to be slightly larger, which is consistent with the sintering detected by XRD. In other sections, filamentous carbon had grown and fragmented the material (Fig. 10, and Fig. S15 and S16). It grew from the edges of the catalyst particles and large whiskers entrapped sizable nickel aggregates, similarly to the unpromoted catalyst. In most cases, the nickel particles in those carbon filaments were detached from the Mg/Al oxides, but in other cases Mg and Al were still mixed with nickel. The nickel particles at the end of the carbon filaments seemed free of carbon, but the nickel aggregates at the tip of the large whiskers were entirely covered in carbon. Some sections of the surface were covered with a layer or amorphous or turbostratic

carbon, similarly to the unpromoted catalyst.

The spent catalysts were investigated by TGA-MS to further assess the characteristics of the carbon structures formed based on their oxidation temperatures (Fig. 11). The unpromoted catalyst presented a mass loss of 35 % from 300 to 620 °C, although mass increased to 102 % at 400 °C by the oxidation of Ni overlapping with the oxidation of the most reactive carbon species. The formation of carbon dioxide presented several overlapping peaks with maxima located at ca. 410, 460, and 580 °C. The first two peaks can be attributed to aliphatic carbon deposits, disordered aromatic structures, and carbon forming nickel carbides and interacting with the Ni-support interfaces, while the higher temperature peak corresponds to more ordered carbon deposits, graphitic carbon filaments, and whiskers [20,23,25–28,48,50]. Therefore, the peaks below 500 °C probably correspond to the gasification of amorphous and disordered aromatic carbon formed by the ketonization and condensation of LA and AGL, while the higher temperature peak corresponds to the graphitic carbon filaments and ordered carbon deposits, in agreement with the results of the Raman spectrum and HR-TEM imaging. The mass loss of HT450/Zr-U9 was close to 54 %, showing that carbon deposition was higher than in the unpromoted material. Most of the carbon combusted between 500 and 660 °C with a single maximum at 625 °C, which corresponds to the temperature of combustion of graphitic filaments [26,50]. This agrees with the massive presence of filaments observed by HR-TEM and indicates little presence of disordered and aliphatic carbon as inferred from the Raman spectrum. Promotion with Zr was thus detrimental since it gave lower surface area and a poorer nickel dispersion with larger nickel particles (Table 2), which favored the growth of filamentous carbon and reduced the rate of reforming [89] resulting on the disintegration of the catalyst by the filaments. Carbon deposition was also higher in HT450/Ce4-U9 than in the unpromoted catalyst, with a mass loss of 50 % during TGA. However, combustion shifted to lower temperature (290 to 590 °C) with a maximum at 520 °C and a shoulder at 390 °C. This is consistent with the lesser presence of graphitic carbon filaments and suggests that aliphatic and disordered aromatic carbon deposits were dominant. Addition of CeO_2 improved the dispersion of nickel due to the interaction between nickel and ceria. It enhanced de redox properties of the surface due to the high Ce^{3+}/Ce^{4+} ratio and created oxygen vacancies in the vicinity of the nickel crystallites [90], while its fluorite structure, in which the oxygen atoms are all in a plane with one another, facilitated a rapid diffusion of the oxygen vacancies near the nickel crystallites [91]. The vacancies led to a higher local availability of adsorbed water, which in turn enhanced the rate of steam reforming and reduced the rate of growth of the graphitic filaments [30,90], which was also inhibited by the small particle size of the nickel crystallites.

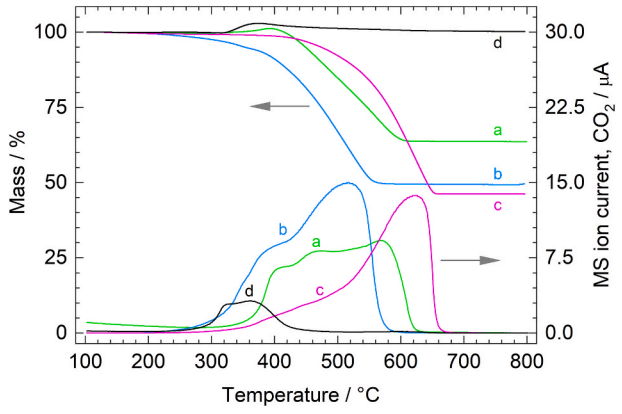


Fig. 11. Carbon combustion in air by TGA-MS analysis of the spent catalysts. Percentage of mass loss and CO_2 signal of the MS detector vs. sample temperature: HT450-U8.4 (a), HT450/Ce4-U8.4 (b), and HT450/Zr-U8.4 (c) after 16 h of TOS at 500°C and a S/C ratio of 8.4, and catalyst HT450/Ce4-U8.4–100 (d) after 100 h of TOS at 600 °C and a S/C ratio of 8.4.

3.2.3. *Extended catalyst stability test*

The HT450/Ce4-R catalyst was selected for an extended activity test of 100 h under constant conditions at atmospheric pressure, S/C of 8.4, and a levulinic acid WHSV of 6.47 h^{-1}. In this case, a reaction temperature of 600 °C was used since a higher reforming temperature significantly decreases the extension of coking. A complete conversion of levulinic acid and a stable performance of the catalyst were observed throughout the experiment (Fig. 12). The average fractional yield of hydrogen was 0.91, with a selectivity to carbon dioxide, carbon monoxide and methane of 0.83, 0.11 and 0.01, respectively. The carbon balance closure was 0.96, with a stable value along the experiment. XRD of the spent catalyst (Fig. 6) showed a broad and weak signal of graphitic carbon, together with a more intense signal of Ni^0 than in the unused catalyst and the presence of a NiO phase (Fig. 2), which could be attributed to sintering. The deposition of carbon was assessed by HR-TEM imaging (Fig. 13 and Fig. S17). Most of the catalyst presented the same structure than the unused catalyst, although the nickel particles were larger thus confirming the occurrence of sintering. Some carbon was deposited throughout the surface without the presence of filamentous structures. In some zones, the structure of the spent catalyst had been disrupted by the formation of compact aggregates of carbon that contained very large particles of nickel, and those were almost free of aluminum and magnesium oxides (Fig. S17). Analysis of the spent catalyst by TGA-MS revealed that the amount of carbon on the catalyst was small. The mass increase caused by the oxidation of nickel

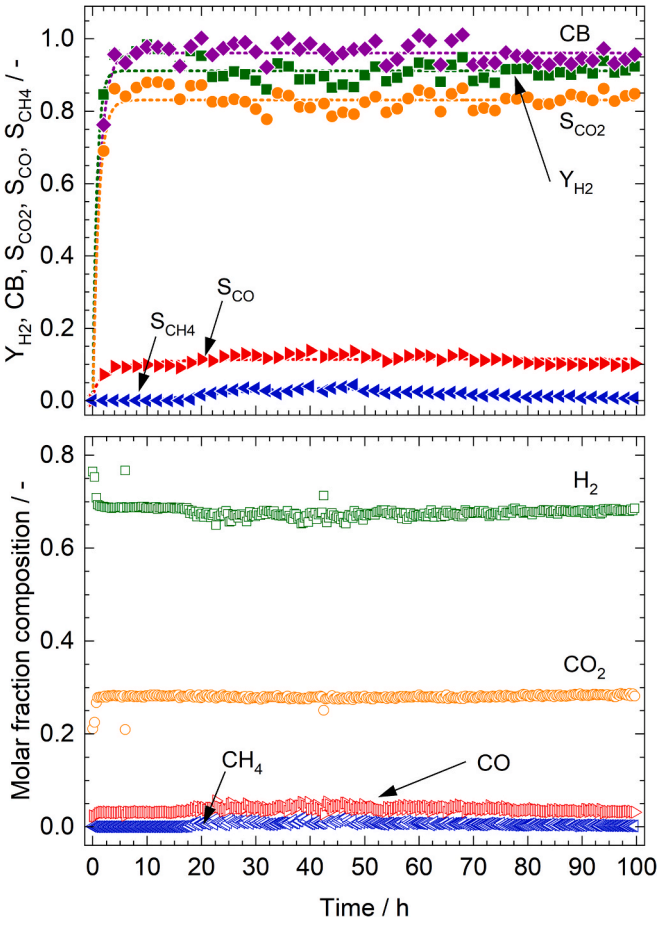


Fig. 12. Lifetime test of HT450/Ce4-R at atmospheric pressure, 600 °C, S/C ratio of 8.4, and a WHSV of 6.47 h^{-1}. Top: hydrogen yield, carbon balance and selectivity to carbon dioxide, carbon monoxide, and methane. Bottom: dry gas mole fraction composition.

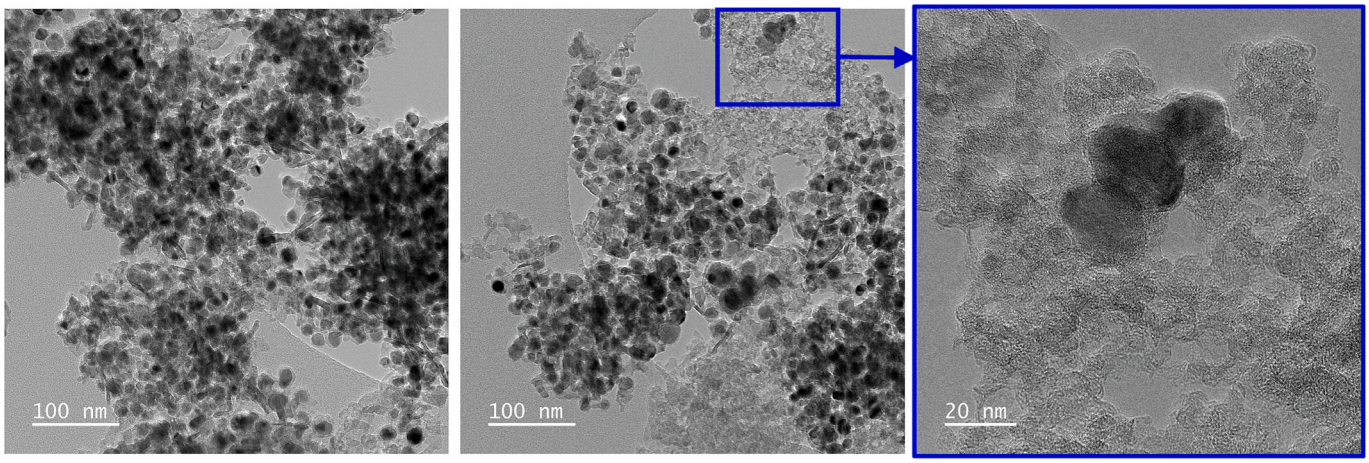


Fig. 13. HR-TEM of two samples of the spent HT411/Ce4-U8.4–100 catalyst after 100 h of TOS at 600 °C, a S/C ratio of 8.4, and a WHSV of 6.47 h^{-1} (see Fig. S14 for EDX element mapping).

compensated the mass loss by the oxidation of carbon, as demonstrated by the small peak of CO_2 recorded by the MS detector. The carbon was oxidized between 300 and 400 °C implying that the observed aggregates consisted mostly of amorphous carbon, which were probably formed by condensation of AGL and LA in areas of the catalyst where the availability of adsorbed water was insufficient to gasify the carbon deposits. Even if the catalyst was relatively clean of carbon, char powder was also collected from the packed bed and separated from the catalyst with a magnet. The char was analyzed by HR-TEM/EDX (Fig. S18). It consisted of massive carbon particles containing nickel particles of 50 – 100 nm attached to a few carbon filaments and to small fragments of catalyst retaining its original morphology. The formation of the char particles seemed to evolve from the aggregates of amorphous carbon, which probably grew over time to form carbon particles that entrapped nickel and small fragments of catalyst. Those grew into dense and non-filamentous particles of char with sizes in the scale of micrometers.

Carbon deposition at 600 °C after 100 h of TOS was much lower than in the same catalyst tested at 500 °C for only 16 h, which shows that temperature had a positive role on the performance of the catalyst. Temperature enhanced the rate of steam reforming over the rates of growth of carbon filaments and disordered graphitic deposits and increased the rate of carbon gasification, but the formation of carbon aggregates that evolved into char particles could not be totally suppressed. During the 100 h of the experiment pressure rose by ca. 1 bar due to the accumulation of char in the bed. Even if the activity of the catalyst was maintained during the test, these results indicate that coking would eventually lead to the destruction of the catalyst after extended time on stream.

4. Conclusions

Steam reforming of levulinic acid, a model compound of the aqueous phase produced from the hydrothermal liquefaction of biomass, was studied using Ni-Mg-Al catalysts obtained from an hydrotalcite-like precursor. The precursor was synthesized by coprecipitation and had a Ni:Mg:Al nominal atomic ratio of 2:1:1. The conditions of calcination and the use of Zr and Ce as activators were assessed. The main conclusions of the work can be summarized in the following points:

- The temperature of calcination influenced the reducibility of the catalysts and their activity. The unpromoted material calcined at 450 °C and reduced at 600 °C gave better selectivity to hydrogen and carbon dioxide and less carbon deposition during the 16 h TOS screening tests than the samples calcined at higher temperature. This was attributed to a better dispersion of nickel in the catalyst calcined at 450 °C, and to a larger presence of weak basic sites that favored the adsorption of water and enhanced reforming and char gasification.
- The steam-to-carbon ratio also played a significant role. A S/C of 2.4, although higher than the minimum requirement to prevent the formation of thermodynamically stable carbon (ca. 1.6 at 500 °C), was too low and resulted in unstable operation due to the rapid accumulation of carbon in the packed bed. Consequently, a S/C of 8.4 was chosen for most of the experiments, including the 100 h stability test with the Ce-promoted catalyst at 600 °C. This S/C is substantially lower than the values of 12 and 24 used at 800 °C on the two published works on the SR of LA available [54,55].
- Promotion of the catalyst with zirconium (Ni:Mg:Al:Zr nominal atomic ratio of 2:1:0.95:0.05) made the material harder to reduce, especially after calcination at 750 °C, and resulted on a poor dispersion of nickel. Even if Zr increased the conversion of LA, the yield of hydrogen, and the selectivity to carbon dioxide, the deposition of carbon was substantial, and sintering of the metal phase was observed, even at a reforming temperature of 500 °C. Promotion of the calcined HT450 precursor with cerium (0.40 atom %) improved the dispersion of nickel upon reduction and facilitated the diffusion of oxygen vacancies, resulting on less sintering and a higher stability of the catalyst.
- Carbon deposition on the catalysts resulted from the combination of three mechanisms: i) diffusion of carbon into the nickel crystallites followed by nucleation and filament growth, ii) dehydrogenation of CH_n promoters, surface migration and growth of encapsulating graphitic structures, and iii) formation of disordered pyrolytic carbon from the products evolving from the ketonization and condensation of LA and AGL. Varying proportions of aliphatic carbon, disordered aromatic carbon, and graphitic carbon deposits were present in the catalysts tested at 500 °C. Promotion with Zr induced the formation of carbon filaments as the main mechanism of coking due to the poor dispersion of nickel. Promotion with Ce favored the formation of aliphatic and disordered aromatic carbon and diminished the formation of filaments. Reforming at 600 °C and S/C of 8.4 substantially inhibited the deposition of carbon.
- An extended test demonstrated a stable operation of the HT450-Ce4-R for 100 h TOS at 600 °C, S/C 8.4 and a levulinic acid WHSV of 6.47 h^{-1}. A 91 % yield of hydrogen and an 83 % selectivity to carbon dioxide were achieved. However, although the catalyst was relatively free of carbon deposits, a substantial amount of char particles accumulated in the packed bed. These char particles trapped fragments of the catalyst and nickel aggregates, suggesting that they originated from the carbon initially deposited on the catalyst.

CRediT authorship contribution statement

Sergi López: Writing – review & editing, Writing – original draft, Visualization, Validation, Methodology, Investigation, Data curation. **Francesc Xavier Lara:** Writing – review & editing, Validation, Investigation, Data curation. **Francesc Medina:** Writing – review & editing, Supervision, Resources, Methodology, Funding acquisition, Conceptualization. **Magdalena Constantí:** Writing – review & editing, Supervision, Resources, Funding acquisition. **Daniel Montané:** Writing – review & editing, Writing – original draft, Visualization, Supervision, Methodology, Data curation, Conceptualization.

Declaration of competing interest

The authors declare that they have no known competing financial interests or personal relationships that could have appeared to influence the work reported in this paper.

Acknowledgments

This research was supported by the Ministry of Science and Innovation (Spain), grant PID2021-123665OB-I00 funded by MCIN/AEI/10.13039/50110001103 and "ERDF A way of making Europe", the Ministry of Ecological Transition and Demographic Challenge (Spain) with NextGenerationEU funds (Val2H2 project R-H2CVAL4-C1-2022-0096), and by the project 2023 CLIMA 00076 funded by AGAUR (Departament de recerca i universitats, Departament d'acció climàtica, alimentació i agenda rural, i el Fons climàtic de la Generalitat de Catalunya, Spain). The authors and the URV would like to thank project EQC2021-007785-P, awarded by the Ministry of Science and Innovation (Spain) and funded by the European Union (NextGenerationEU), for the total funding for the acquisition of the XPS system (ProvenX-NAP from SPECS) at the SRCiT of the URV. The authors thank Dr. Anton Dafinov (TGA) and Dr. Daniel Ruano (XPS) for their technical assistance, and Susana Domínguez for administrative support.

Appendix A. Supplementary data

Supplementary data to this article can be found online at https://doi.org/10.1016/j.fuel.2025.137354.

Data availability

Data will be made available on request.

References

[1] Vardon DR, Sharma BK, Blazina GV, Rajagopalan K, Strathmann TJ. Thermochemical conversion of raw and defatted algal biomass via hydrothermal liquefaction and slow pyrolysis. Bioresour Technol 2012;109:178–87. https://doi.org/10.1016/j.biortech.2012.01.008.
[2] Kumar R, Strezov V. Thermochemical production of bio-oil: a review of downstream processing technologies for bio-oil upgrading, production of hydrogen and high value-added products. Renew Sust Energ Rev 2021;135:110152. https://doi.org/10.1016/j.rser.2020.110152.
[3] Gollakota ARK, Kishore N, Gu S. A review on hydrothermal liquefaction of biomass. Renew Sustain Energ Rev 2018;81:1378–93. https://doi.org/10.1016/j.rser.2017.05.178.
[4] Usman M, Cheng S, Boonyubol S, Cross JS. From biomass to biocrude: Innovations in hydrothermal liquefaction and upgrading. Energ Convers Manage 2024;302:118093. https://doi.org/10.1016/j.enconman.2024.118093.
[5] Dimitriadis A, Bezergianni S. Hydrothermal liquefaction of various biomass and waste feedstocks for biocrude production: a state of the art review. Renew Sust Energ Rev 2017;68:113–25. https://doi.org/10.1016/j.rser.2016.09.120.
[6] Dong S, Liu Z, Yang X. Exploration of hydrothermal liquefaction of multiple algae to improve bio-crude quality and carbohydrate utilization. Appl Energ 2024;361:122861. https://doi.org/10.1016/j.apenergy.2024.122861.
[7] Jena H, Das KC. Comparative evaluation of thermochemical liquefaction and pyrolysis for bio-oil production from microalgae. Energ Fuel 2011;25:5472–82. https://doi.org/10.1021/ef201373m.
[8] Doassans-Carrère N, Ferrasse J-H, Boutin O, Mauviel G, Léde J. Comparative study of biomass fast pyrolysis and direct liquefaction for bio-oils production: products yield and characterizations. Energ Fuel 2014;28:5103–11. https://doi.org/10.1021/ef500641c.
[9] Saber M, Nakhshiniev B, Yoshikawa K. A review of production and upgrading of algal bio-oil. Renew Sustain Energ Rev 2016;58:918–30. https://doi.org/10.1016/j.rser.2015.12.342.
[10] Diebold JP. A review of the chemical and physical mechanisms of the storage stability of fast pyrolysis bio-oils. NREL/SR-570-27613, National Renewal Energy. Laboratory 2000.
[11] Kim TS, Kim J-Y, Kim K-H, Lee S, Choi D, Choi I-G, et al. The effect of storage duration on bio-oil properties. J Annal Appl Pyrol 2012;95:118–25. https://doi.org/10.1016/j.jaap.2012.01.015.
[12] Chen D, Zhou J, Zhang Q, Zhu X. Evaluation methods and research progresses in bio-oil storage stability. Renew Sustain Energ Rev 2014;40:69–79. https://doi.org/10.1016/j.rser.2014.07.159.
[13] Wang Y, Zhang Y, Yoshikawa K, Li H, Liu Z. Effect of biomass origins and composition on stability of hydrothermal biocrude oil. Fuel 2021;302:121138. https://doi.org/10.1016/j.fuel.2021.121138.
[14] Gomez-Castro FI, Gutierrez Antonio C, Romero-Izquierdo AG, May-Vazquez MM, Hernandez S. Intensified technologies for the production of triglyceride-based biofuels: current status and future trends. Renew Sustain Energ Rev 2023;184:113580. https://doi.org/10.1016/j.rser.2023.113580.
[15] Tzanetis KF, Posada JA, Ramirez A. Analysis of biomass hydrothermal liquefaction and biocrude-oil upgrading for renewable jet fuel production: the impact of reaction conditions on production costs and GHG emissions performance. Renew Energ 2017;113:1388–98. https://doi.org/10.1016/j.renene.2017.06.104.
[16] Wang D, Czernik S, Montané D, Mann M, Chornet E. Biomass to hydrogen via fast pyrolysis and catalytic steam reforming of the pyrolysis oil or its fractions. Ind Eng Chem Res 1997;36:1507–18. https://doi.org/10.1021/ie960396g.
[17] Lepage T, Kammoun M, Schmetz Q, Richel A. Biomass-to-hydrogen: a review of main routes production, processes evaluation and techno-economical assessment. Biomass Bioenerg 2021;144:105920. https://doi.org/10.1016/j.biombioe.2020.105920.
[18] Davidson SD, Lopez-Ruiz JA, Zhu Y, Cooper AR, Albrecht KO, Dagle RA. Strategies to valorize the hydrothermal liquefaction-derived aqueous phase into fuels and chemicals. ACS Sustain Chem Eng 2019;7:19889–901. https://doi.org/10.1021/acssuschemeng.9b05308.
[19] Li X, Zhang Z, Zhang L, Fan H, Li X, Liu Q, et al. Investigation of coking behaviors of model compounds in bio-oil during steam reforming. Fuel 2020;265:116961. https://doi.org/10.1016/j.fuel.2019.116961.
[20] Landa L, Remiro A, Valecillos J, Valle B, Bilbao J, Gayubo AG. Unveiling the deactivation by coke of $NiAl_2O_4$ spinel derived catalysts in the bio-oil steam reforming: Role of individual oxygenates. Fuel 2022;321:124009. https://doi.org/10.1016/j.fuel.2022.124009.
[21] Zhang S, Li X, Li Q, Xu Q, Yan Y. Hydrogen production from the aqueous phase derived from fast pyrolysis of biomass. J Anal Appl Pyrol 2011;92:158–63. https://doi.org/10.1016/j.jaap.2011.05.007.
[22] Remón J, Broust F, Volle G, García L, Arauzo J. Hydrogen production from pine and poplar bio-oils by catalytic steam reforming. Influence of the bio-oil composition on the process. Int J Hydrogen. Energ 2015;40:5593–608. https://doi.org/10.1016/j.ijhydene.2015.02.117.
[23] Ochoa A, Aramburu B, Valle B, Resasco DE, Bilbao J, Gayubo AG, et al. Role of oxygenates and effect of operating conditions in the deactivation of a Ni supported catalyst during the steam reforming of bio-oil. Green Chem 2017;19:4315–33. https://doi.org/10.1039/c7gc01432e.
[24] Bimbela F, Oliva M, Ruiz J, García L, Arauzo J. Hydrogen production by catalytic steam reforming of acetic acid, a model compound of biomass pyrolysis liquids. J Anal Appl Pyrol 2007;79:112–20. https://doi.org/10.1016/j.jaap.2006.11.006.
[25] Xing R, Dagle VL, Flake M, Kovarik L, Albrecht KO, Deshmane C, et al. Steam reforming of fast pyrolysis-derived aqueous phase oxygenates over Co, Ni, and Rh metals supported on $MgAl_2O_4$. Catal Today 2016;269:166–74. https://doi.org/10.1016/j.cattod.2015.11.046.
[26] Zhang A, Li Z, Yi W, Fu P, Wang L, Liang C, et al. Study the reaction mechanism of catalytic reforming of acetic acid through the instantaneous gas production. Int J Hydrogen Energ 2019;44:21279–89. https://doi.org/10.1016/j.ijhydene.2019.06.060.
[27] Fu P, Zhang A, Luo S, Yi W, Zhang Y. Comparative study on the catalytic steam reforming of biomass pyrolysis oil and its derivatives for hydrogen production. RSC Adv 2020;10:12721–9. https://doi.org/10.1039/d0ra01409e.
[28] Guo W, Li G, Zheng Y, Li K, Guo L. Influence of La_2O_3 addition on activity and coke formation over Ni/SiO_2 for acetic acid steam reforming. Int J Hydrogen Energ 2022;47:3633–43. https://doi.org/10.1016/j.ijhydene.2021.11.023.
[29] Bimbela F, Oliva M, Ruiz J, García L, Arauzo J. Hydrogen production via catalytic steam reforming of the aqueous fraction of bio-oil using nickel-based coprecipitated catalysts. Int J Hydrogen Energ 2013;38:14476–87. https://doi.org/10.1016/j.ijhydene.2013.09.038.
[30] Hoang TMC, Geerdink B, Sturm JM, Lefferts L, Seshan K. Steam reforming of acetic acid – a major component in the volatiles formed during gasification of humin. Appl Catal B-Environ 2015;163:74–82. https://doi.org/10.1016/j.apcatb.2014.07.046.
[31] Goicoechea S, Kraleva E, Sokolov S, Schneider M, Pohl M-M, Kockmann N, et al. Support effect on structure and performance of Co and Ni catalysts for steam reforming of acetic acid. Appl Catal A-Gen 2016;514:182–91. https://doi.org/10.1016/j.apcata.2015.12.025.
[32] Bimbela F, Ábrego J, Puerta R, García L, Arauzo J. Catalytic steam reforming of the aqueous fraction of bio-oil using Ni-Ce/Mg-Al catalysts. Appl Catal B-Environ 2017;209:346–57. https://doi.org/10.1016/j.apcatb.2017.03.009.

[33] Zhao X, Xue Y, Yan C, Huang Y, Lu Z, Wang Z, et al. Promoted activity of porous silica coated Ni/CeO_2–ZrO_2 catalyst for steam reforming of acetic acid. Int J Hydrogen Energ 2017;42:21677–85. https://doi.org/10.1016/j.ijhydene.2017.07.086.

[34] Bizkarra K, Bermudez JM, Arcelus-Arrillaga P, Barrio VL, Cambra JF, Millan M. Nickel based monometallic and bimetallic catalysts for synthetic and real bio-oil steam reforming. Int J Hydrogen Energ 2018;43:11706–18. https://doi.org/10.1016/j.ijhydene.2018.03.049.

[35] Choi I-H, Hwang K-R, Lee K-Y, Lee I-G. Catalytic steam reforming of biomass-derived acetic acid over modified Ni/γ-Al_2O_3 for sustainable hydrogen production. Int J Hydrogen Energ 2019;44:180–90. https://doi.org/10.1016/j.ijhydene.2018.04.192.

[36] Santamaria L, Artetxe M, Lopez G, Cortazar M, Amutio M, Bilbao J, et al. Effect of CeO_2 and MgO promoters on the performance of a Ni/Al_2O_3 catalyst in the steam reforming of biomass pyrolysis volatiles. Fuel Process Technol 2020;198:106223. https://doi.org/10.1016/j.fuproc.2019.106223.

[37] Wang Z, Sun L, Chen L, Yang S, Xie X, Gao M, et al. Steam reforming of acetic acid for hydrogen production over Ni/Ca_xFe_yO catalysts. Int J Hydrogen Energ 2021;46:33132–42. https://doi.org/10.1016/j.ijhydene.2021.07.145.

[38] Singh PP, Jaswal A, Nirmalkar N, Mondal T. Synergistic effect of transition metals substitution on the catalytic activity of $LaNi_{0.5}M_{0.5}O_3$ (M = Co, Cu, and Fe) perovskite catalyst for steam reforming of simulated bio-oil for green hydrogen production. Renew. Energ 2023;207:575–87. https://doi.org/10.1016/j.renene.2023.03.057.

[39] Yan Y, Lin M, Jiang D, Li R, Song X, Wu Y. Influences of Ni/CeO_2 morphologies on steam reforming for acetic acid – a model compound of bio-oil. Int J Hydrogen Energ 2024;73:362–72. https://doi.org/10.1016/j.ijhydene.2024.05.383.

[40] Basagiannis AC, Verykios XE. Reforming reactions of acetic acid on nickel catalysts over a wide temperature range. Appl Catal A-Gen 2006;308:182–93. https://doi.org/10.1016/j.apcata.2006.04.024.

[41] Liu C, Hongmanorom P, Ashok J, Chen D, Wu Q, Wang W, et al. An effect blending of acetone and acetic acid as bio-oil model compound for steam reforming reaction over Ce doped $LaNi_{0.8}Fe_{0.2}O_3$-based perovskite. Biomass Bioenerg 2021;151:106177. https://doi.org/10.1016/j.biombioe.2021.106177.

[42] Davidson SD, Spies KA, Mei D, Kovarik L, Kutnyakov I, Li XS, et al. Steam reforming of acetic acid over co-supported catalysts: coupling ketonization for greater stability. ACS Sustain Chem Eng 2017;5:9136–49. https://doi.org/10.1021/acssuschemeng.7b02052.

[43] Zhang F, Wang M, Zhu L, Wang S, Zhou J, Luo Z. A comparative research on the catalytic activity of La_2O_3 and -Al_2O_3 supported catalysts for acetic acid steam reforming. Int J Hydrogen Energ 2017;42:3667–75. https://doi.org/10.1016/j.ijhydene.2016.06.264.

[44] Santamaria L, Lopez G, Arregi A, Artetxe M, Amutio M, Bilbao J, et al. Catalytic steam reforming of biomass fast pyrolysis volatiles over Ni–Co bimetallic catalysts. J Ind Eng Chem 2020;91:167–81. https://doi.org/10.1016/j.jiec.2020.07.050.

[45] Fu P, Zhang A, Luo S, Yi W, Hu S, Zhang Y. Catalytic steam reforming of biomass-derived acetic acid over two supported Ni catalysts for hydrogen-rich syngas production. ACS Omega 2019;4:13585–93. https://doi.org/10.1021/acsomega.9b01985.

[46] Argyle MD, Bartholomew CH. Heterogeneous catalyst deactivation and regeneration: a review. Catalysts 2015;5:145–269. https://doi.org/10.3390/catal5010145.

[47] Valle B, Remiro A, Aguayo AT, Bilbao J, Gayubo AG. Catalysts of Ni/ -Al_2O_3 and Ni/La_2O_3- Al_2O_3 for hydrogen production by steam reforming of bio-oil aqueous fraction with pyrolytic lignin retention. Int J Hydrogen Energ 2013;38:1307–18. https://doi.org/10.1016/j.ijhydene.2012.11.014.

[48] Remiro A, Valle B, Aguayo AT, Bilbao J, Gayubo AG. Operating conditions for attenuating Ni/La_2O_3– Al_2O_3 catalyst deactivation in the steam reforming of bio-oil aqueous fraction. Fuel Process Technol 2013;115:222–32. https://doi.org/10.1016/j.fuproc.2013.06.003.

[49] Lee SC, Choi JH, Lee CW, Woo SH, Lee J, Woo HC. H_2 production by steam reforming of Saccharina japonica-derived liquefied oils on Ni_xCu_y hydrotalcite-derived catalysts. Renew Energ 2022;191:418–27. https://doi.org/10.1016/j.renene.2022.03.161.

[50] Park YB, Choi JH, Lee SC, Lee CW, Woo SH, Lee J, et al. Boosting hydrogen production by reducible oxygen species over Ni/MTi_xO_y catalysts for the steam reforming of liquefied oil from *Saccharina japonica*. Fuel Process Technol 2022;238:107486. https://doi.org/10.1016/j.fuproc.2022.107486.

[51] Lu J, Li X, Yang R, Zhao J, Liu Y, Qu Y. Liquefaction of fermentation residue of reed- and corn stover-pretreated with liquid hot water in the presence of ethanol with aluminum chloride as the catalyst. Chem Eng J 2014;247:142–51. https://doi.org/10.1016/j.cej.2014.02.094.

[52] Lee JH, Hwang H, Moon J, Choi JW. Characterization of hydrothermal liquefaction products from coconut shell in the presence of selected transition metal chlorides. J Anal Appl Pyrol 2016;122:415–21. https://doi.org/10.1016/j.jaap.2016.11.005.

[53] Lee JH, Hwang H, Choi JW. Effects of transition metals on hydrothermal liquefaction of empty fruit bunches (EFB) for conversion to biofuel and valuable chemicals. Energy 2018;162:1–9. https://doi.org/10.1016/j.energy.2018.07.197.

[54] Li T, Su H, Zhu L, Xu D, Ji N, Wang S. Hydrogen production from steam reforming of biomass-derived levulinic acid over highly stable spinel-supported Ni catalysts. Waste Dispos Sustain Energ 2023;5:427–38. https://doi.org/10.1007/s42768-023-00154-2.

[55] Su H, Li T, Zhu L, Xu G, Wang S. Catalytic steam reforming of aqueous products derived from hydrothermal conversion of biomass for hydrogen production. Resour Chem Mater 2025;4:100121. https://doi.org/10.1016/j.recm.2025.100121.

[56] Biesinger MC. Accessing the robustness of adventitious carbon for charge referencing (correction) purposes in XPS analysis: Insights from a multi-user facility data review. Appl Surf Sci 2022;597:15368. https://doi.org/10.1016/j.apsusc.2022.153681.

[57] Biesinger MC, Payne BP, Grosvenor AP, Lau LWM, Gerson AR, Smart RStC. Resolving surface chemical states in XPS analysis of first row transition metals, oxides and hydroxides: Cr, Mn, Fe, Co and Ni. Appl Surf Sci 2011;257:2717-2730 Doi: 10.1016/j.apsusc.2010.10.051.

[58] Schierbaum KD. Ordered ultra-thin cerium oxide overlayers on Pt(111) single crystal surfaces studied by LEED and XPS. Surf Sci 1998;399:29–38. https://doi.org/10.1016/S0039-6028(97)00808-X.

[59] Burroughs P, Hamnett A, Orchard AF, Thornton G. Satellite structure in the X-ray photoelectron spectra of some binary and mixed oxides of lanthanum and cerium. J Chem Soc Dalton Trans 1976:1686–98. https://doi.org/10.1039/DT9760001686.

[60] Ridler DE, Twigg MV. Steam reforming. Chapter 5. In: Twigg MV, editor. Catalyst Handbook, 2nd ed., London: Wolfe Publishing Ltd; 1989, p. 225-282.

[61] Rostrup-Nielsen JR, Sehested J, Nørskov JK. Hydrogen and synthesis gas by steam- and CO_2 reforming. Adv Catal 2002;47:65–139. https://doi.org/10.1016/S0360-0564(02)47006-X.

[62] Rostrup-Nielsen JR, Sehested J. Whisker carbon revisited. Stud Surf Sci Catal 2001;139:1–12. https://doi.org/10.1016/S0167-2991(01)80174-9.

[63] Bengaard HS, Nørskov JK, Sehested J, Clausen BS, Nielsen LP, Molenbroek AM, et al. Steam reforming and graphite formation on Ni catalysts. J Catal 2002;209:365–84. https://doi.org/10.1006/jcat.2002.3579.

[64] Thommes M, Kaneko K, Neimark AV, Olivier JP, Rodriguez-Reinoso F, Rouquerol J, et al. Physisorption of gases, with special reference to the evaluation of surface area and pore size distribution (IUPAC Technical Report). Pure Appl Chem 2015;87:1051–69. https://doi.org/10.1515/pac-2014-1117.

[65] Meis NNAH, Bitter JH, de Jong KP. Support and size effects of activated hydrotalcites for precombustion CO_2 capture. Ind Eng Chem Res 2010;49:1229–35. https://doi.org/10.1021/ie901114d.

[66] Yang W, Kim Y, Liu PKT, Sahimi M, Tsotsis TT. A study by in situ techniques of the thermal evolution of the structure of a Mg–Al–CO_3 layered double hydroxide. Chem Eng Sci 2002;57:2945–53. https://doi.org/10.1016/s0009-2509(02)00185-9.

[67] Fedorova ZA, Borisov VA, Pakharukova VP, Gerasimov EY, Belyaev VD, Gulyaeva TI, et al. Layered double hydroxide-derived Ni-Mg-Al catalysts for ammonia decomposition process: synthesis and characterization. Catalysts 2023;13:678. https://doi.org/10.3390/catal13040678.

[68] Hibino T, Yamashita Y, Kosuge K, Tsunashima A. Decarbonation behavior of Mg-Al-CO_3 hydrotalcite-like compounds during heat treatment. Clay Clay Miner 1995;43:427–32. https://doi.org/10.1346/ccmn.1995.0430405.

[69] Summa P, Świrk K, Wierzbicki D, Motak M, Alxneit I, Rønning M, et al. Coprecipitated Ni-Mg-Al hydrotalcite-derived catalyst promoted with vanadium for CO_2 methanation. Molecules 2021;26:6506. https://doi.org/10.3390/molecules26216506.

[70] Daza CE, Cabrera CR, Moreno S, Molina R. Syngas production from CO_2 reforming of methane using Ce-doped Ni-catalysts obtained from hydrotalcites by reconstruction method. Appl Catal A-Gen 2010;378:125–33. https://doi.org/10.1016/j.apcata.2010.01.037.

[71] Wierzbicki D, Baran R, Dębek R, Motak M, Grzybek T, Gálvez ME, et al. The influence of nickel content on the performance of hydrotalcite-derived catalysts in CO_2 methanation reaction. Int J Hydrogen Energ 2017;42:23548–55. https://doi.org/10.1016/j.ijhydene.2017.02.148.

[72] Dębek R, Motak M, Galvez ME, Grzybek T, Da Costa P. Influence of Ce/Zr molar ratio on catalytic performance of hydrotalcite-derived catalysts at low temperature CO_2 methane reforming. Int J Hydrogen Energ 2017;42:23556–67. https://doi.org/10.1016/j.ijhydene.2016.12.121.

[73] Bolognini M, Cavani F, Scagliarini D, Flego C, Perego C, Saba M. Heterogeneous basic catalysts as alternatives to homogeneous catalysts: reactivity of Mg/Al mixed oxides in the alkylation of m-cresol with methanol. Catal Today 2002;75:103–11. https://doi.org/10.1016/s0920-5861(02)00050-0.

[74] Gac W. Acid–base properties of Ni–MgO–Al_2O_3 materials. Appl Surf Sci 2011;257:2875–80. https://doi.org/10.1016/j.apsusc.2010.10.084.

[75] Kuśtrowski P, Chmielarz L, Bożek E, Sawalha M, Roessner F. Acidity and basicity of hydrotalcite derived mixed Mg–Al oxides studied by test reaction of MBOH conversion and temperature programmed desorption of NH_3 and CO_2. Mater Res Bull 2004;39:263–81. https://doi.org/10.1016/j.materresbull.2003.09.032.

[76] Radlik M, Adamowska-Teyssier M, Krztoń A, Kozieł K, Krajewski W, Turek W, et al. Dry reforming of methane over Ni/$Ce_{0.62}Zr_{0.38}O_2$ catalysts: effect of Ni loading on the catalytic activity and on H_2/CO production. C R Chimie 2015;18:1242–9. https://doi.org/10.1016/j.crci.2015.03.008.

[77] Cavani F, Trifirò F, Vaccari A. Hydrotalcite-type anionic clays: preparation, properties and applications. Catal Today 1991;11:173–301. https://doi.org/10.1016/0920-5861(91)80068-k.

[78] Touahra F, Sehailia M, Ketir W, Bachari K, Chebout R, Trari M, et al. Effect of the Ni/Al ratio of hydrotalcite-type catalysts on their performance in the methane dry reforming process. Appl Petrochem Res 2015;6:1–13. https://doi.org/10.1007/s13203-015-0109-y.

[79] Montero C, Ochoa A, Castaño P, Bilbao J, Gayubo AG. Monitoring Ni^0 and coke evolution during the deactivation of a Ni/La_2O_3– Al_2O_3 catalyst in ethanol steam reforming in a fluidized bed. J Catal 2015;331:181–92. https://doi.org/10.1016/j.jcat.2015.08.005.

[80] Xue Q, Li Z, Yi H, Jiang Z, Yan B, Wang Y, et al. Controlling sintering and carbon deposition with post-coated MgO confined group VIII metal-based catalysts

towards durable high-temperature steam reforming. Appl Catal B-Environ 2022; 318:121874. https://doi.org/10.1016/j.apcatb.2022.121874.
[81] Xiao Z, Zhang C, Huang S, Zhang S, Tan X, Lian Z, et al. A comprehensive review on steam reforming of liquid hydrocarbon fuels: Research advances and prospects. Fuel 2024;368:131596. https://doi.org/10.1016/j.fuel.2024.131596.
[82] Sun D, Takahashi Y, Yamada Y, Sato S. Efficient formation of angelica lactones in a vapor-phase conversion of levulinic acid. Appl Catal A-Gen 2016;526:62–9. https://doi.org/10.1016/j.apcata.2016.07.025.
[83] Juárez P, López-Aguado C, Paniagua M, Melero JA, Mariscal R, Morales G. Self-condensation of levulinic acid into bio-jet fuel precursors over acid zeolites: Elucidating the role of nature, strength and density of acid sites. Appl Catal A-Gen 2022;631:118480. https://doi.org/10.1016/j.apcata.2022.118480.
[84] Zhang X, Li Y, Qian C, An L, Wang W, Li X, et al. Research progress of catalysts for aldol condensation of biomass based compounds. RSC Adv 2023;13:9466–78. https://doi.org/10.1039/d3ra00906h.
[85] Lilga MA, Padmaperuma AB, Auberry DL, Job HM, Swita MS. Ketonization of levulinic acid and -valerolactone to hydrocarbon fuel precursors. Catal Today 2018;302:80–6. https://doi.org/10.1016/j.cattod.2017.06.021.
[86] Pham TN, Sooknoi T, Crossley SP, Resasco DE. Ketonization of carboxylic acids: mechanisms, catalysts, and implications for biomass conversion. ACS Catal 2013;3: 2456–73. https://doi.org/10.1021/cs400501h.
[87] Karimi E, Freitas Teixeira I, Passos Ribeiro L, Gomez A, Lago RM, Penner G, et al. Ketonization and deoxygenation of alkanoic acids and conversion of levulinic acid to hydrocarbons using a Red Mud bauxite mining waste as the catalyst. Catal Today 2012;190:73–88. https://doi.org/10.1016/j.cattod.2011.11.028.
[88] Kumar R, Enjamuri N, Shah S, Al-Fatesh AS, Bravo-Suárez JJ, Chowdhury B. Ketonization of oxygenated hydrocarbons on metal oxide based catalysts. Catal Today 2012;190:16–49. https://doi.org/10.1016/j.cattod.2017.09.044.
[89] Zhou F, Pan N, Chen H, Xu X, Wang C, Du Y, et al. Hydrogen production through steam reforming of toluene over Ce, Zr or Fe promoted Ni-Mg-Al hydrotalcite-derived catalysts at low temperature. Energ Convers Manage 2019;196:677–87. https://doi.org/10.1016/j.enconman.2019.06.047.
[90] Rached JA, El Hayek C, Dahdah E, Gennequin C, Aouad S, Tidahy HL, et al. Ni based catalysts promoted with cerium used in the steam reforming of toluene for hydrogen production. Int J Hydrogen Energ 2017;42:12829–40. https://doi.org/10.1016/j.ijhydene.2016.10.053.
[91] Pérez Zurita MJ, Bartolini M, Righi T, Vitale G, Pereira AP. Hydrotalcite type materials as catalyst precursors for the catalytic steam cracking of toluene. Fuel 2015;154:71–9. https://doi.org/10.1016/j.fuel.2015.03.002.